RESEARCH ARTICLE SUMMARY

IMMUNOLOGY

Regulatory T cells constrain T cells of shared specificity to enforce tolerance during infection

David E. J. Klawon†, Nicole Pagane†, Matthew T. Walker, Nicole K. Ganci, Christine H. Miller, Eric Gai, Donald M. Rodriguez, Bridgett K. Ryan-Payseur, Ryan K. Duncombe, Erin J. Adams, Mark Maienschein-Cline, Nancy E. Freitag, Ronald N. Germain*, Harikesh S. Wong*, Peter A. Savage*

INTRODUCTION: A fundamental feature of the adaptive immune system is its ability to generate immunity to foreign pathogens while restricting collateral damage to self-tissues, a property referred to as self-nonself discrimination. In the T cell compartment, this effect is conferred in part by the purging or inactivation of conventional T (T_{conv}) cells exhibiting strong reactivity to self-peptides complexed with host major histocompatibility complex (MHC) molecules (self-pMHC). However, despite these mechanisms, self-pMHC–reactive T_{conv} cells with pathogenic potential persist, requiring continuous control by Foxp3-expressing regulatory T (T_{reg}) cells to prevent autoimmunity.

RATIONALE: This observation highlights a fundamental unanswered question that sits at the nexus of protective immunity and autoimmunity: During infection, in which both self- and pathogen-derived peptides are presented in an inflammatory environment permissive for T cell activation, how do T_{reg} cells selectively control T_{conv} cells reactive to self-peptides while simultaneously enabling robust T cell responses to pathogen-derived peptides? Conventional modes of T_{reg} cell suppression—such as sequestration of costimulatory ligands, local hoarding of secreted factors, and production of suppressive cytokines—function broadly without regard to the peptide specificity of responding T cells. Therefore, these mechanisms lack the selectivity needed to distinguish between self- and nonself-reactive T_{conv} cells. To address this gap, we examined the hypothesis that T_{reg} cells reactive to self-peptides selectively constrain T_{conv} cells of matched specificity during infection, thereby enforcing self-nonself discrimination.

RESULTS: Through the study of $CD4^+$ T cell responses to a natural prostate-specific self-peptide, we identified two tiers of T_{reg} cell–mediated regulation. T_{reg} cells of matched specificity were not required for the control of self-peptide–reactive T_{conv} cells at steady state or after innate immune activation. However, such T_{reg} cells became crucial in a setting of pathogen-associated epitope mimicry, in which levels of both innate activation and self-peptide presentation rise concurrently. When self-peptide–specific T_{reg} cells were present, mice were protected from autoimmunity after infection with a bacterium expressing the self-peptide. In the absence of such T_{reg} cells, infection induced extensive autoimmunity of the prostate. T_{reg} cells reactive to the self-peptide did not prevent the priming of T_{conv} cells of shared specificity but instead stifled their subsequent proliferation and differentiation. The expansion of self-peptide–reactive T_{reg} cells occurred earlier than that of T_{conv} cell counterparts, suggesting that antigen-activated T_{reg} cells were intrinsically poised to accumulate more rapidly, thereby providing a numerical advantage in the early stages of the response. Quantitative imaging revealed heterogeneous patterns of T_{reg} cell–mediated control; some self-pMHC–specific T_{conv} cells were restrained by locally enriched polyclonal T_{reg} cells, whereas others required the local enrichment of T_{reg} cells of shared specificity to attenuate T cell receptor (TCR) and interleukin-2 (IL-2) signaling, thereby stifling proliferation and effector differentiation. Notably, T_{reg} cell–mediated control of self-peptide–reactive T_{conv} cells had no impact on the T_{conv} cell response to pathogen-derived nonself peptides, demonstrating self-peptide specificity of the observed suppression.

CONCLUSION: The selective control of self-peptide–reactive T_{conv} cells by T_{reg} cells of matched specificity may be especially relevant for immunological insults that are proposed drivers of autoimmunity, including pathogen-associated epitope mimicry or the release of self-antigens and inflammatory signals triggered by infection-induced cell death. These findings support a T_{reg} cell–centric model of self-nonself discrimination in which the immune system generates T_{reg} cells reactive to highly antigenic self-peptide ligands, selectively focusing immunosuppression on T_{conv} cells of matched specificity during strong immunological challenges. This model complements and advances classical paradigms of self-nonself discrimination, illustrating how the adaptive immune system operates on a knife's edge between effective pathogen control and the risk of autoimmunity during infection. ■

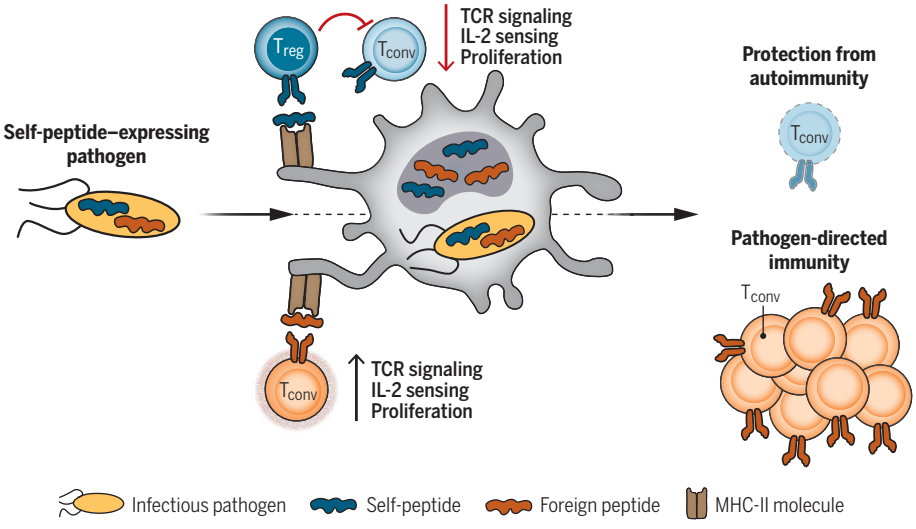

T_{reg} cells enforce self-nonself discrimination during infection by selectively constraining T_{conv} cells of shared self-specificity. Upon infection with a pathogen expressing a self-peptide—a model of pathogen-associated epitope mimicry or elevated self-antigen elicited by tissue damage—self-peptide–specific T_{reg} cells selectively control $CD4^+$ T_{conv} cells reactive to the same peptide by attenuating TCR stimulation, IL-2 signaling, and proliferation. This selective suppression simultaneously prevents autoimmunity and enables robust T_{conv} responses against foreign pathogen–derived peptides to protect the host.

The list of author affiliations is available in the full article online.
*Corresponding author. Email: psavage@bsd.uchicago.edu (P.A.S.); wonghs@mit.edu (H.S.W.); rgermain@niaid.nih.gov (R.N.G.)
†These authors contributed equally to this work.
Cite this article as D. E. J. Klawon *et al.*, *Science* **387**, eadk3248 (2025). DOI: 10.1126/science.adk3248

READ THE FULL ARTICLE AT
https://doi.org/10.1126/science.adk3248

RESEARCH ARTICLE

IMMUNOLOGY

Regulatory T cells constrain T cells of shared specificity to enforce tolerance during infection

David E. J. Klawon[1]†‡, Nicole Pagane[2,3]‡, Matthew T. Walker[1], Nicole K. Ganci[1], Christine H. Miller[1,4]§, Eric Gai[2,3], Donald M. Rodriguez[1,4], Bridgett K. Ryan-Payseur[5], Ryan K. Duncombe[6], Erin J. Adams[6], Mark Maienschein-Cline[7], Nancy E. Freitag[8], Ronald N. Germain[9]*, Harikesh S. Wong[2,10]*, Peter A. Savage[1]*

During infections, CD4$^+$ Foxp3$^+$ regulatory T (T_{reg}) cells must control autoreactive CD4$^+$ conventional T (T_{conv}) cell responses against self-peptide antigens while permitting those against pathogen-derived "nonself" peptides. We defined the basis of this selectivity using mice in which T_{reg} cells reactive to a single prostate-specific self-peptide were selectively depleted. We found that self-peptide–specific T_{reg} cells were dispensable for the control of T_{conv} cells of matched specificity at homeostasis. However, they were required to control such T_{conv} cells and prevent autoimmunity toward the prostate after exposure to elevated self-peptide during infection. Notably, the T_{reg} cell response to self-peptide did not affect protective T_{conv} cell responses to a pathogen-derived peptide. Thus, self-peptide–specific T_{reg} cells promoted self-nonself discrimination during infection by selectively controlling T_{conv} cells of shared self-specificity.

Most conventional αβ T cells recognize short peptide antigens bound to host major histocompatibility complex molecules (pMHCs) displayed on the surface of antigen-presenting cells (APCs). Such recognition is mediated by a heterodimeric αβ T cell receptor (TCR), which is generated by a quasi-random gene recombination process during T cell development in the thymus (*1*). This process establishes a diverse peripheral pool of T cell clones, each expressing a distinct TCR. Protective host defense requires the elicitation of rare T cell clones exhibiting strong reactivity to pathogen-derived peptides, which undergo activation, proliferation, and effector T cell differentiation. However, the establishment of a diverse T cell repertoire introduces immunological risk, as some generated TCRs may react strongly to MHC molecules complexed with peptides derived from self-expressed proteins (self-peptides; self-pMHCs), potentially promoting host autoimmunity (*2*). This necessitates a range of control mechanisms that limit T cell responses against self-constituents, innocuous substances, and commensal microbes while enabling those against nonself threats.

The earliest form of control operates in the thymus to delete some developing T cells exhibiting strong TCR reactivity toward self-pMHCs, including those derived from peripheral tissue–restricted antigens (*3*, *4*). However, some highly self-reactive T cell clones have been demonstrated to seed the peripheral repertoire, including self-reactive CD4$^+$ T_{conv} cells with the potential to differentiate into effector cells capable of triggering or potentiating autoimmunity (*5*–*10*). These escapees are controlled by Foxp3$^+$ T_{reg} cells—a specialized CD4$^+$ T cell subset whose differentiation is also triggered in part by strong reactivity to self-pMHCs in the thymus (*11*) and which are required throughout life to control highly self-reactive T_{conv} cells in the periphery, thereby preventing autoimmunity (*12*).

T_{reg} cells use multiple mechanisms to achieve this outcome, including masking or removal of costimulatory ligands on the surface of APCs, absorption of T cell growth factors such as interleukin-2 (IL-2), and production of suppressive cytokines that restrict the differentiation of T_{conv} cells or modulate their priming by APCs (*13*–*18*). These mechanisms can operate at one or more stages of T cell activation and effector differentiation, functioning to raise T_{conv} cell activation thresholds and/or limit the progression of ongoing T_{conv} cell responses through negative feedback. In this regard, recent work suggests that at steady state, T_{reg} cells do not prevent the activation and cytokine production of many self-reactive T_{conv} cells (*19*) but instead coordinate local feedback control to dampen nascent self-reactive T_{conv} cell responses in the secondary lymphoid organs (SLOs) (*20*).

The ongoing activation of rare T_{conv} cells by self-pMHCs in SLOs raises a conceptual conundrum related to T_{reg} cell function during inflammatory conditions such as infection. Infection-associated tissue damage may increase TCR signaling and costimulation in self-reactive T_{conv} cells owing to the release of self-antigens and inflammatory signals from dying cells. Furthermore, pathogen-derived peptides can exhibit topological similarities to self-peptides, potentially increasing TCR signaling in some self-pMHC–reactive T_{conv} clones during infection. This phenomenon, referred to as epitope mimicry (*21*, *22*), has been proposed as a driver of some autoimmune diseases. Consistent with this idea, a recent report identified T cell clones expanded in human autoimmune lesions that cross-react with both self-peptides and microbial peptides (*23*).

Infection thus presents a singular challenge: T_{reg} cells must permit useful T_{conv} cell responses against pathogen-derived peptides while simultaneously constraining self-reactive T_{conv} cells, which may receive both heightened TCR signals and increased costimulation from activated APCs. If unchecked, this potential for enhanced signaling could saturate the capacity of T_{reg} cells to coordinate immunosuppression (*16*, *24*, *25*). Yet overt autoimmune disease is rarely observed in the context of infection, suggesting that T_{reg} cells can selectively control T_{conv} cell responses against self-peptides while simultaneously permitting those directed against nonself-peptides. One mechanism that could account for this type of discrimination relates to shared self-pMHC specificities of some T_{reg} cells and T_{conv} cells. Several studies have documented the coexistence of mature T_{reg} and T_{conv} cells that recognize the same self-pMHCs within the endogenous repertoires of healthy mice (*26*–*31*) and humans (*32*), raising the possibility that self-pMHC–specific T_{reg} cells may preferentially regulate T_{conv} cells of matched specificity. Previous studies have demonstrated that the infusion of large numbers of in vitro–generated pMHC-specific T_{reg} cells can selectively regulate T_{conv} cell responses of shared specificity to foreign (*33*), self (*34*), and microbial peptides (*35*), but it remains unknown whether such principles are operative for naturally occurring T_{reg} cell populations reactive to endogenous self-peptides. On the basis of these collective observations, we examined the hypothesis that T_{reg} cells reactive

[1]Department of Pathology, University of Chicago, Chicago, IL, USA. [2]The Ragon Institute of Mass General, MIT and Harvard, Cambridge, MA, USA. [3]Program in Computational and Systems Biology, Massachusetts Institute of Technology, Cambridge, MA, USA. [4]Interdisciplinary Scientist Training Program, University of Chicago, Chicago, IL, USA. [5]Department of Microbiology and Immunology, University of Illinois Chicago, Chicago, IL, USA. [6]Department of Biochemistry and Molecular Biology, University of Chicago, Chicago, IL, USA. [7]Research Informatics Core, Research Resources Center, University of Illinois Chicago, Chicago, IL, USA. [8]Department of Pharmaceutical Sciences, University of Illinois Chicago, Chicago, IL, USA. [9]Lymphocyte Biology Section, Laboratory of Immune System Biology, National Institute of Allergy and Infectious Diseases, National Institutes of Health, Bethesda, MD, USA. [10]Department of Biology, Massachusetts Institute of Technology, Cambridge, MA, USA.
***Corresponding author. Email: psavage@bsd.uchicago.edu (P.A.S.); wonghs@mit.edu (H.S.W.); rgermain@niaid.nih.gov (R.N.G.)**
†Present address: Koch Institute for Integrative Cancer Research, Massachusetts Institute of Technology, Cambridge, MA, USA.
‡These authors contributed equally to this work.
§Present address: Department of Pathology, University of California, San Francisco, School of Medicine, San Francisco, CA, USA.

to self-pMHCs selectively constrain T_{conv} cells of matched specificity while permitting T_{conv} cell responses to pathogen-derived peptides, thereby promoting self-nonself discrimination during infection.

Results

C4-specific MJ23 T_{conv} cells are activated by self-peptide at steady state and trigger the local enrichment of polyclonal T_{reg} cells

We set up a mouse model system to analyze $CD4^+$ T cell responses to a natural self-peptide called C4, which is derived from the prostate-specific protein Tcaf3 and displayed by the MHC class II molecule I-A^b. The Tcaf3 protein and its derivative peptides are recurrently targeted by autoantibodies and T_{conv} cells, respectively, in settings of immune dysregulation (*26*, *36*, *37*). C4/I-A^b complexes are presented in the thymus, through Aire-dependent mechanisms, thereby directing a fraction of developing C4-specific T cells into the T_{reg} cell lineage (*38*, *39*) without inducing measurable clonal deletion (*40*) (fig. S1A). In contrast, C4 is not required in the thymus for the positive selection of C4-reactive T_{conv} cells, consistent with the known degeneracy of TCR recognition of pMHCs and the need for only low levels of TCR signaling for effective T_{conv} cell positive selection. The net result is a mixture of C4-specific T_{reg} and T_{conv} cells in the mature peripheral T cell repertoire (fig. S1A). The C4-specific T cell response can be studied using fluorescent C4/I-A^b tetramers (*39*) and monoclonal T cells from TCR transgenic mice expressing the C4-specific MJ23 TCR (MJ23tg mice) (*38*). Tcaf3 also yields a second nonoverlapping I-A^b–restricted peptide called F1, which, like C4, facilitates Aire-dependent T_{reg} cell differentiation in the thymus (*26*, *39*) and is recognized by antigen-specific T_{reg} cells in the prostate-draining lymph nodes (pLNs) (fig. S1A). Thus, the Tcaf3 system enables the study of naturally occurring T_{reg} cell populations reactive to two distinct self-peptides derived from a single source protein.

To determine whether the control of C4-specific T_{conv} cells requires T_{reg} cells of matched specificity at homeostasis, we adoptively transferred naïve MJ23 T_{conv} cells from female MJ23tg *Rag1*$^{-/-}$ $CD45^{.1/.1}$ mice into healthy male recipients (Fig. 1A), which harbor endogenous C4/I-A^b–specific T_{reg} cells (*39*). Twenty-four hours after transfer, donor MJ23 T_{conv} cells in the pLNs up-regulated Egr2, a marker of TCR signaling (*41*), and the cell cycle–related protein Ki67 (*42*) (fig. S1, B to D). In line with recent findings (*20*), at this same time point, multiplexed confocal imaging of the pLNs revealed local enrichment of T_{reg} cells around MJ23 T_{conv} cells expressing programmed cell death protein 1 (PD-1) (Fig. 1, B and C), an inhibitory receptor whose expression scales as a function of TCR signaling intensity (*20*). Cotransferred polyclonal T_{conv} cells, by contrast, did not trigger this local enrichment of T_{reg} cells (Fig. 1C). At later time points, MJ23 T_{conv} cells exhibited increased Ki67 expression (fig. S1D) and modestly elevated frequencies in the pLNs at day 3 after transfer, before returning to or falling below baseline frequencies at day 14 (Fig. 1D and fig. S1E). At all measured time points, most MJ23 T_{conv} cells in the pLNs failed to adopt an anergic phenotype, a dysfunctional state that limits the activity of self-specific T_{conv} cells and is characterized by elevated expression of the surface markers FR4 and CD73 ($FR4^{hi}$ $CD73^{hi}$) (fig. S1, F and G) (*10*). These findings demonstrate that T_{reg} cells within the endogenous repertoire do not prevent MJ23 T_{conv} cells from sensing C4/I-A^b ligand, becoming activated, and entering the cell cycle. Instead, these results suggest that T_{reg} cells might exert local feedback control, surrounding the activated T_{conv} cells to form microdomains that stifle nascent effector responses, a phenomenon that has been reported previously (*20*, *43*).

The formation of microdomains requires T_{reg} cell TCR engagement of pMHCs on APCs (*19*, *20*), consistent with the need for TCR signaling by T_{reg} cells to prevent autoimmunity (*44*, *45*). We generated MJ23tg bone marrow chimeric (BMC) male mice (Fig. 1E), which harbor a mixture of MJ23 T_{reg} and T_{conv} cells at low frequencies within a polyclonal T cell repertoire (*38*), and quantified the activation status of MJ23 T_{reg} cells compared with T_{conv} cells and assessed the spatial localization of MJ23 T_{reg} cells with respect to MJ23 T_{conv} cells. We used MJ23 T cells expressing the *Foxp3*$^{DTR\text{-}EGFP}$ allele (*12*) to ablate $Foxp3^+$ MJ23 T_{reg} cells through administration of diphtheria toxin (DT) (Fig. 1F and fig. S1H). In unmanipulated MJ23 BMC males, a fraction of both MJ23 T_{reg} and T_{conv} cells actively sensed ligand in the pLNs, as measured by Erg2 expression (Fig. 1, G and H), but not the spleen (fig. S1, I and J) at steady state. These findings confirmed that C4/I-A^b ligand was accessible for T cell recognition at homeostasis in this system and indicated that most peripheral MJ23 T_{conv} cells were not irreversibly inactivated by prior residence in male mice. T_{reg} cells selectively accumulated around activated MJ23 T_{conv} cells compared with nonactivated $CD4^+$ T_{conv} cells sampled at random within the same pLN paracortex (Fig. 1I). However, the resulting microdomains were devoid of MJ23 T_{reg} cells (Fig. 1J). Ablation of MJ23 T_{reg} cells through DT administration did not alter the percentage of MJ23 T_{conv} cells expressing Egr2 (Fig. 1H). These analyses indicate that C4/I-A^b is readily accessible for recognition by both MJ23 T_{conv} cells and T_{reg} cells at steady state and that MJ23 T_{reg} cells do not measurably colocalize with MJ23 T_{conv} cells nor play a detectable role in limiting their recognition of C4/I-A^b ligand in this setting.

C4-specific T_{conv} cells are controlled by polyclonal T_{reg} cells in settings of innate activation

To further assess the role of T_{reg} cells in controlling T_{conv} cells of matched self-pMHC specificity in a natural polyclonal repertoire, we engineered mice in which exon 5 of the *Tcaf3* gene, which encodes the region containing the C4 epitope, was flanked by loxP sites (fig. S2A). Crossing these mice to *Foxn1*-Cre^+ mice (*46*) yielded offspring in which *Tcaf3* exon 5 was selectively deleted in thymic epithelial cells (TECs), leaving *Tcaf3* and C4 peptide expression in the prostate unaltered [*Foxn1*-Cre^+ *Tcaf3(ex5)*$^{flox/flox}$ mice, hereafter referred to as $C4^{\Delta TEC}$ mice] (Fig. 2A). This alteration was designed to impair the selection of C4/I-A^b–specific T_{reg} cells in the thymus without altering the selection of T_{reg} cells reactive to other self-pMHCs. In this setting, mature C4-specific T cells were heavily skewed toward the T_{conv} fate in the periphery (fig. S2, B to E).

In the absence of immune challenge, $C4^{\Delta TEC}$ mice did not develop spontaneous T cell infiltration of the prostate at 4, 6, and 12 months of age (fig. S2, F and G). Treatment of $C4^{\Delta TEC}$ mice with C4 peptide alone (fig. S2, H to M) or agonists of innate signaling pathways known to activate APCs, including anti-CD40 agonist antibody, lipopolysaccharide (LPS), or polyinosinic:polycytidylic acid (poly I:C) (fig. S2, N to R), also failed to induce prostatic T_{conv} cell infiltration. We also examined control of self-specific T_{conv} cells during bacterial infection by challenging $C4^{\Delta TEC}$ males with an attenuated parental strain of *Listeria monocytogenes* (*Lm[parent]*), a common bacterial pathogen that triggers multiple innate signaling pathways (*47*–*52*). Although *Lm* propagates predominantly in the spleen and liver when injected intravenously (*53*), we observed activation of polyclonal $CD4^+$ T_{conv} cells in distal SLOs, including the pLNs (fig. S3, A to D), consistent with systemic inflammation. However, despite such distal APC activation, infection of $C4^{\Delta TEC}$ males with a virulent strain of *Lm[parent]* did not cause C4-specific T_{conv} cells to break tolerance and infiltrate the prostate (fig. S3, E to G). This result was not explained by loss of C4 presentation in the pLNs, as newly transferred MJ23 T_{conv} cells were activated to the same extent compared with homeostatic conditions (fig. S3D) (*54*). Collectively, these results suggested that C4/I-A^b-specific T_{conv} cells did not break tolerance in the absence of matched T_{reg} cells, even after APC activation by a variety of inflammatory signals or after provision of antigenic peptide alone.

Thymic presentation of C4/I-A^b is required to prevent prostatitis after Lm[C4] infection and does not affect the T cell response to the Lm-derived LLO peptide

Proposed drivers of autoimmunity include scenarios in which self-specific T_{conv} cells perceive

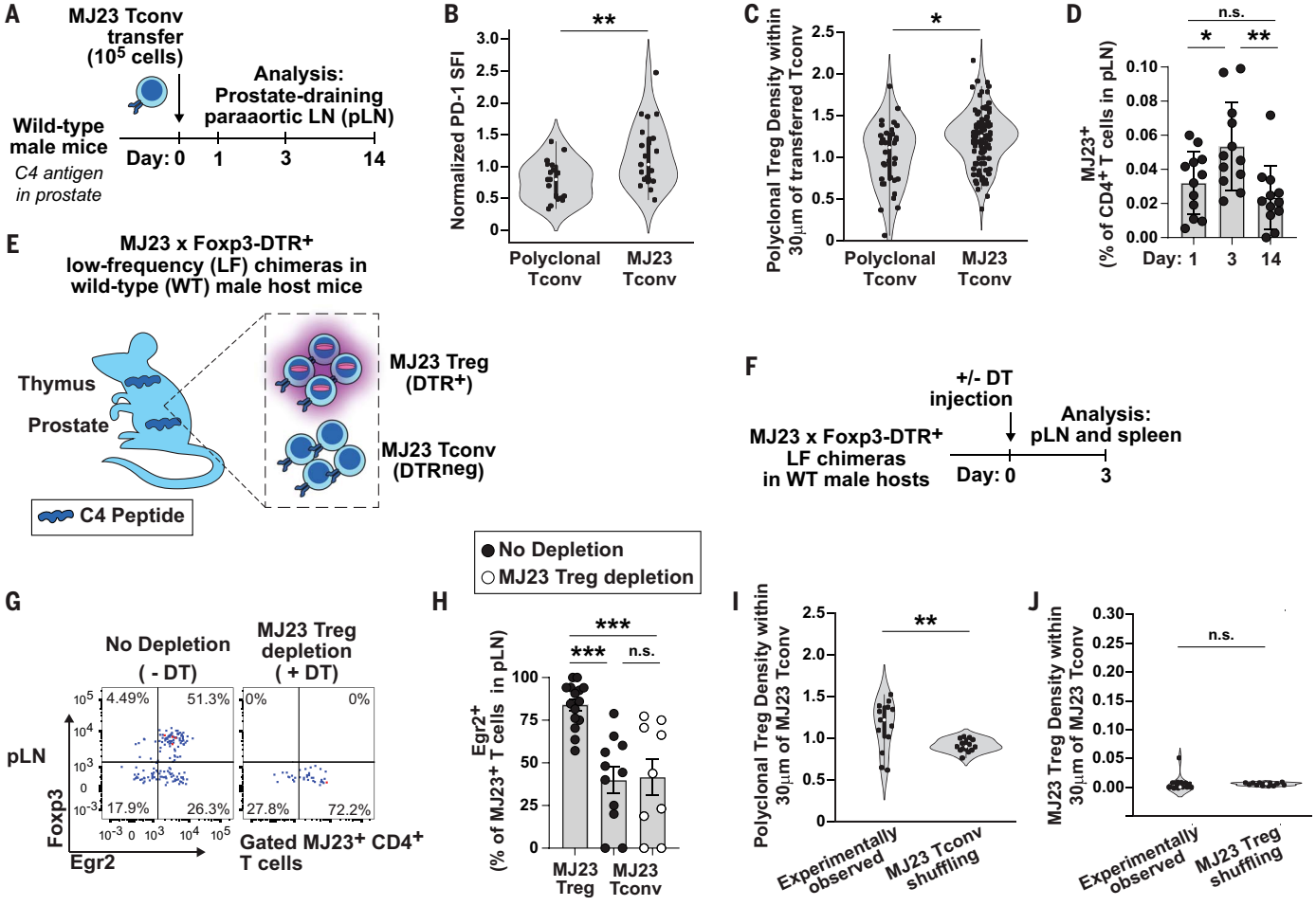

Fig. 1. C4-specific MJ23 T_{conv} cells are activated by self-ligand at steady state and trigger the local enrichment of polyclonal T_{reg} cells. (**A**) Experimental schematic for (B) to (D). (**B**) Summary of PD-1 mean fluorescence intensity (MFI) on transferred MJ23 or polyclonal T_{conv} cells 24 hours after transfer, as determined by confocal microscopy. n = 18, polyclonal T_{conv}; n = 23, MJ23 T_{conv}. (**C**) Local scaled density of polyclonal T_{reg} cells within a 30-μm radius of MJ23 T_{conv} cells or transferred polyclonal T_{conv} cells 24 hours after transfer, as determined by confocal imaging. n = 34, polyclonal T_{conv}; n = 107, MJ23 T_{conv}. (**D**) Frequency of MJ23$^+$ CD4$^+$ T_{conv} cells among polyclonal CD4$^+$ T cells in the pLNs at the indicated time point after transfer, identified by flow cytometry. n = 12, d1; n = 12, d3; n = 12, d14. (**E** and **F**) Wild-type male mice were irradiated and reconstituted with a low frequency of congenically disparate MJ23tg$^+$ *Rag1*$^{-/-}$ *Foxp3*^{DTR} bone marrow (LF MJ23 chimeric mice). More than six weeks after engraftment the fate of MJ23 T cells was assessed in the pLNs by flow cytometry or confocal microscopy. LF MJ23 chimeras were depleted of MJ23 T_{reg} cells by diphtheria toxin injection (DT) 3 days before analysis or left untreated. (**G**) Representative flow cytometric analysis of Egr2 versus Foxp3 expression by MJ23 CD4$^+$ T cells isolated from the pLNs. The frequency of cells within gates is denoted. (**H**) Frequency of Egr2$^+$ cells among MJ23 CD4$^+$ T_{reg} and T_{conv} cells isolated from the pLNs of host mice, measured by flow cytometry. n = 20, no depletion; n = 10, MJ23 T_{reg} depletion. (**I** and **J**) pLNs were harvested from untreated LF MJ23 chimeric mice as in (F) and analyzed by confocal microscopy. The observed local scaled density of polyclonal (I) or MJ23 (J) T_{reg} cells within a 30-μm radius of each MJ23 T_{conv} cell was determined and was compared with the density after the positions of MJ23 T_{conv} and MJ23 T_{reg} cells were randomly shuffled with polyclonal T_{conv} and T_{reg} cells, respectively. For (I), n = 13, shuffled, and n = 13, observed; for (J), n = 13, shuffled, and n = 13, observed. Flow cytometric gating strategy is described in fig. S13. The n values and individual data points shown in graphs represent the number of cells [(B), (C), (I), and (J)] or the number of mice [(D) and (H)]. Data are pooled from multiple independent experiments: n = 2 [(B) and (C)], n = 3 (D), n = 4 or 5 [(G) and (H)], n = 2 [(I) and (J)]. Graphs show mean and quartiles [(B), (C), (I), and (J)] or mean ± SEM [(D) and (H)]. P values were calculated by two-tailed nonparametric Mann-Whitney test [(B) and (C)], ordinary one-way analysis of variance (ANOVA) [(D) and (H)], or as described in the Materials and methods [(I) and (J)] [*P < 0.05; **P < 0.01; ***P < 0.001; not significant (n.s.) = P > 0.05].

both innate activation and elevated TCR signals, including pathogen-associated epitope mimicry and settings in which the quantity of self-pMHC ligands is increased by infection-associated cell death. To model these settings, we engineered the attenuated *Lm[parent]* strain to express recombinant C4 peptide (*Lm[C4]*). In wild-type males that received CellTrace Violet–labeled MJ23 T_{conv} cells, challenge with *Lm[C4]* drove the robust proliferation and expansion of MJ23 T_{conv} cells at the major site of *Lm* propagation (fig. S4A). Thus, infection with the *Lm[C4]* strain enabled the study of temporally synchronized C4-specific T_{conv} cell responses in an inflammatory environment associated with elevated presentation of the C4 self-peptide. Of note, peptide/I-A^b tetramers can be used to track the CD4$^+$ T cell responses to both the C4 self-peptide and the natural I-A^b–restricted *Lm*-derived peptide $LLO_{190-201}$ (LLO, listeriolysin O) (Fig. 2B), which serves as a pathogen-derived foreign epitope with no known self-peptide analog.

To define whether T_{reg} cells reactive to C4 played a role in controlling T_{conv} cells of matched specificity and maintaining tolerance in this setting, we infected *C4*^{WT} and *C4*$^{\Delta TEC}$ males with *Lm[C4]* and analyzed T cell responses (Fig. 2C). In *C4*^{WT} mice, infection with *Lm[C4]* failed to induce prostatic T cell infiltration

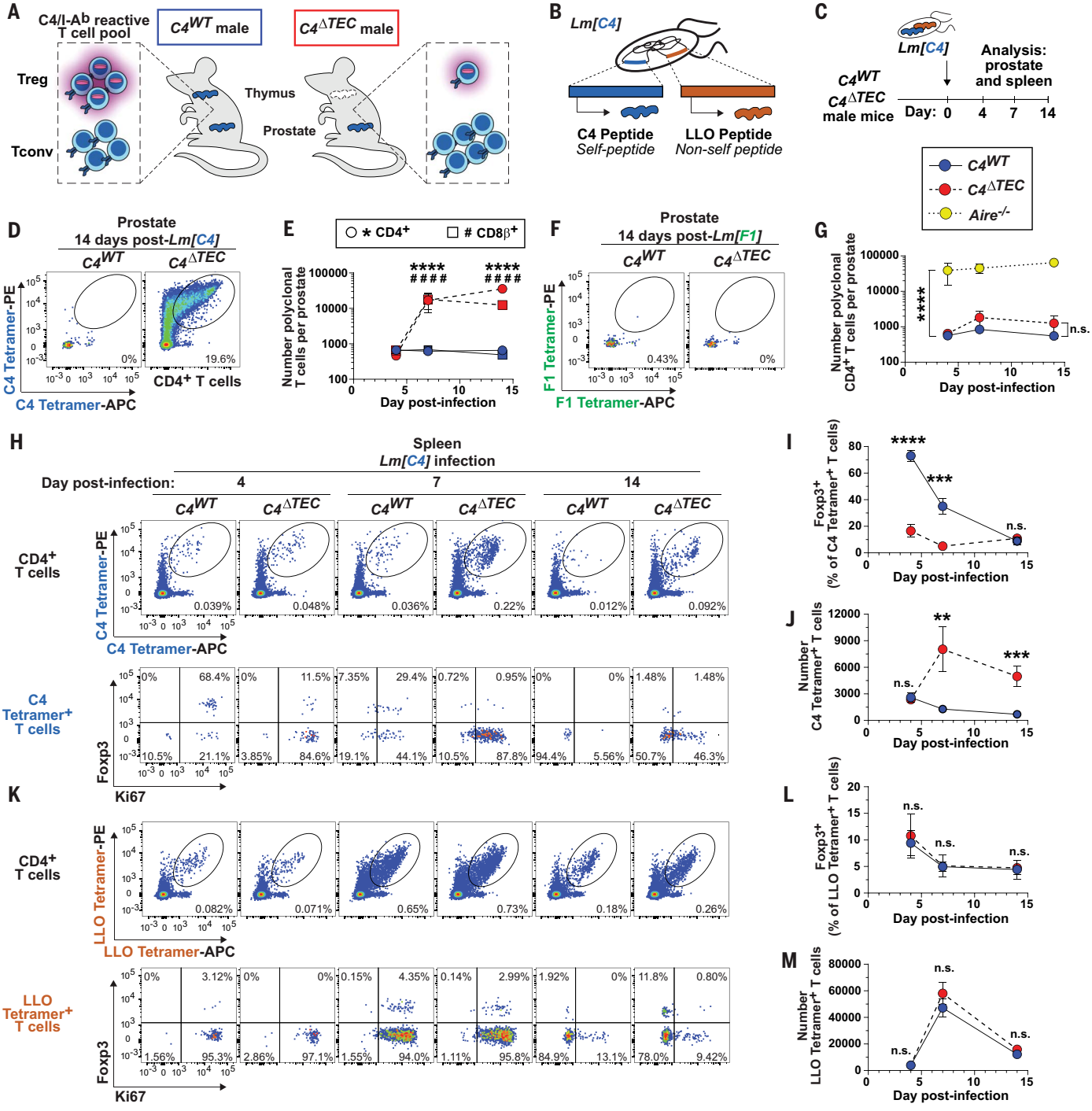

Fig. 2. Thymic presentation of C4/I-A^b is required to prevent prostatitis after *Lm[C4]* infection and does not affect the T cell response to the *Lm*-derived LLO peptide. (**A**) Schematic depicting the anatomical location of C4 peptide expression and the approximate frequencies of endogenous C4/I-A^b–specific T_{reg} and T_{conv} cells in $C4^{WT}$ and $C4^{\Delta TEC}$ male mice. (**B**) Schematic depicting peptide expression in the genetically engineered *Lm[C4]* pathogen strain. (**C**) Experimental design for (D), (E), and (H) to (M). *Lm[C4]*: n = 6, $C4^{WT}$ d4; n = 7, $C4^{\Delta TEC}$ d4; n = 6, $C4^{WT}$ d7; n = 7, $C4^{\Delta TEC}$ d7; n = 8, $C4^{WT}$ d14; n = 10, $C4^{\Delta TEC}$ d14. (**D**) Representative analysis of C4/I-A^b tetramer–APC versus –PE expression by polyclonal CD4$^+$ T cells after infection with *Lm[C4]*. The frequency of cells within gates is denoted. (**E**) Summary plot of the number of CD4$^+$ T cells and CD8β$^+$ T cells recovered from the prostates of mice. (**F** and **G**) $C4^{WT}$ and $C4^{\Delta TEC}$ mice were challenged intravenously with 10^7 CFU *Lm [F1]*, as in fig. S4F, and T cells isolated from the prostate were analyzed. $Aire^{-/-}$ male mice lacking tolerance to the F1 peptide were infected as a control. n = 4, $C4^{WT}$; n = 4, $C4^{\Delta TEC}$; and n = 2, $Aire^{-/-}$. (F) Representative analysis of F1/I-A^b tetramer–APC versus –PE expression by polyclonal CD4$^+$ T cells. The frequency of cells within the gates are denoted. (G) Pooled data showing the number of CD4$^+$ T cells recovered from the prostates of *Lm[F1]*-challenged mice. (**H** to **M**) Analysis of T cells in the spleen in *Lm[C4]*-challenged mice treated as in (C). (H) Representative analysis of C4/I-A^b tetramer–APC versus –PE expression in polyclonal CD4$^+$ T cells (top) and Ki67 versus Foxp3 expression by C4/I-A^b tetramer$^+$ T cells (bottom). The frequency of cells within gates is denoted. (I) Data pooled from (H) showing the frequency of dual C4/I-A^b tetramer$^+$ CD4$^+$

T cells expressing Foxp3. (J) Pooled data from (H) showing the number of dual C4/I-A^b tetramer$^+$ CD4$^+$ T cells. (K) Representative analysis of LLO/I-A^b tetramer–APC versus –PE expression by polyclonal CD4$^+$ T cells (top) and Ki67 versus Foxp3 expression by LLO/I-A^b tetramer$^+$ T cells (bottom). The frequency of cells within gates is denoted. (L) Pooled data from (K) showing the frequency of dual LLO/I-A^b tetramer$^+$ CD4$^+$ T cells expressing Foxp3. (M) Pooled data from (K) showing the number of dual LLO/I-A^b tetramer$^+$ CD4$^+$ T cells. Flow cytometric gating strategy is described in fig. S13. The *n* values represent the number of mice. Data are pooled from multiple independent experiments: *n* = 3 or 4 [(D) and (E)], *n* = 2 [(F) and (G)], *n* = 3 or 4 [(H) to (M)]. In all graphs, each symbol represents the mean ± SEM of pooled mice. Asterisk symbols denote comparison of CD4$^+$ T cells, and hashtag symbols denote comparison of CD8β$^+$ T cells. *P* values were calculated by two-tailed nonparametric Mann-Whitney test [(E), (I), (J), (L), and (M)] or ordinary two-way ANOVA (G) (*P < 0.05; **P < 0.01; ***P < 0.001; ****P < 0.0001; n.s. = P > 0.05).

(Fig. 2, D and E, and fig. S4, B to E). In contrast, *Lm[C4]* challenge of $C4^{\Delta TEC}$ mice induced extensive T cell infiltration of the prostate by day 14, characterized by a substantial fraction of C4-specific T_{conv} cells (Fig. 2, D and E, and fig. S4, D and E). After challenge with attenuated *Lm* expressing the F1 peptide (*Lm[F1]*), the T cell response to F1 was indistinguishable between $C4^{WT}$ and $C4^{\Delta TEC}$ mice (fig. S4, F to O), and $C4^{\Delta TEC}$ mice were resistant to prostatitis (Fig. 2, F and G). This demonstrated that tolerance to F1 was intact in $C4^{\Delta TEC}$ mice and that C4-specific T_{reg} cells were not required to control the T_{conv} cell response to the linked F1 peptide. In addition, transient T_{reg} depletion of all T_{reg} cells in $C4^{WT}$ $Foxp3^{DTR\text{-}eGFP}$ male mice at the time of *Lm[C4]* challenge triggered prostatitis characterized by infiltration of C4-specific T_{conv} cells (fig. S5). This finding demonstrated that C4-specific T_{conv} cells with pathogenic potential were not specific to $C4^{\Delta TEC}$ males lacking C4 peptide in the thymus; the endogenous repertoire of $C4^{WT}$ males also harbored such cells.

Thus, our findings demonstrate that in a setting of elevated C4 peptide presentation in the context of infection, C4-specific T_{conv} cells induce organ-specific autoimmunity in the absence of T_{reg} cells with matched specificity. In this setting, all other T_{reg} cells, including T_{reg} cells reactive to related self-peptides such as the Tcaf3-derived F1 peptide, are unable to sufficiently control C4-specific T_{conv} cells.

Given the divergent outcomes in $C4^{WT}$ and $C4^{\Delta TEC}$ mice after *Lm[C4]* infection, we sought to characterize the arc of the C4-specific T cell response. The response in $C4^{WT}$ mice, which were protected from prostatitis (Fig. 2D), was characterized by a T_{reg} cell–skewed response that peaked at day 4 in the spleen and waned progressively at days 7 and 14 (Fig. 2, H to J). A major fraction of both C4-specific (C4/I-A^b tetramer$^+$) T_{reg} cells and T_{conv} cells were Ki67$^+$ at day 4 (fig. S4P), indicating that C4-specific T_{conv} cells were primed in $C4^{WT}$ mice in the early days of *Lm[C4]* infection but were ultimately controlled (Fig. 2H). In $C4^{\Delta TEC}$ mice, the C4-specific response was characterized by a T_{conv} cell–skewed response at day 4 (Fig. 2, H and I). Later time points saw the continued expansion of C4/I-A^b tetramer$^+$ T cells in the spleen at day 7 (Fig. 2J) and elevated frequencies of C4-specific T cells in the pLNs (fig. S6, A to D) and prostate (fig. S4E) at days 7 and 14. In parallel, we assessed the response of CD4$^+$ T cells reactive to $LLO_{190\text{-}201}$ (Fig. 2B) and found that the frequency (Fig. 2, K to M) and phenotype (figs. S4Q and S6, E to G) of LLO-specific T cells was indistinguishable between $C4^{WT}$ and $C4^{\Delta TEC}$ mice. Thus, the divergent T cell response to C4 in $C4^{WT}$ compared with $C4^{\Delta TEC}$ mice did not affect the T cell response to a second *Lm*-expressed peptide. These results demonstrate that in $C4^{WT}$ mice, C4-specific T_{reg} cells effectively discriminate between T_{conv} cell responses to self-peptide and those reactive to nonself peptide.

C4-specific T_{reg} cells restrict the emergence of C4-specific T_{conv} cells exhibiting proliferative and stemlike central-memory states during Lm[C4] *infection*

To understand how C4-specific T_{conv} cells were controlled in $C4^{WT}$ mice during *Lm[C4]* infection, we performed single-cell RNA sequencing (scRNA-seq) of C4/I-A^b tetramer$^+$ T cells purified from the spleens of $C4^{WT}$ and $C4^{\Delta TEC}$ mice 4 days after *Lm[C4]* challenge, an early time point at which the C4-specific T cell responses are poised to diverge (Fig. 2J). Uniform manifold approximation and projection (UMAP) with unsupervised clustering revealed 14 distinct T cell clusters (Fig. 3A), none of which were exclusive to the $C4^{WT}$ or $C4^{\Delta TEC}$ settings (Fig. 3B) but instead differed in their proportional representation (fig. S7, A and B). Three clusters (clusters 1 and 9, plus cluster 10 in $C4^{WT}$ only) exhibited expression of *Foxp3* and other T_{reg} cell–defining signature genes (Fig. 3C and fig. S7B). These T_{reg} cells accounted for 61.7% (±5.00% SEM) of C4/I-A^b tetramer$^+$ T cells from $C4^{WT}$ mice but only 5.92% (±1.46% SEM) of cells from $C4^{\Delta TEC}$ mice.

We proceeded to define differences in the transcriptional states adopted by C4-specific T_{conv} cells elicited in *Lm[C4]*-challenged $C4^{WT}$ and $C4^{\Delta TEC}$ mice. Our analysis coalesced around select genes identified as cluster-defining genes for one or more clusters on the basis of differential expression statistics (Fig. 3, D and E). These genes included the *Mki67* gene encoding Ki67; the chemokine receptor–encoding *Ccr2*, *Cxcr6*, and *Ccr7* genes; and the *Tcf7* gene encoding the transcription factor TCF1. High CCR2 and CXCR6 expression are hallmarks of inflammatory effector cells capable of migrating into peripheral tissues, whereas high CCR7 expression is associated with T cell retention in lymphoid tissues (*55*). High expression of TCF1 is a hallmark of "stemlike" central-memory T cells (*56*, *57*), which have been implicated as key reservoirs supporting sustained effector T cell responses in multiple contexts (*58*–*63*).

The most abundant T_{conv} cell cluster enriched in $C4^{WT}$ mice was cluster 5 (Fig. 3E). This cluster was characterized by elevated expression of *Ccr2* and *Cxcr6*, low expression of *Tcf7* and *Ccr7*, and low expression of *Mki67* and other cell cycle–related genes (Fig. 3D and fig. S7B), indicative of short-lived effector cells that had lost proliferative potential. In contrast, T_{conv} cell clusters 4 and 6 were overrepresented in $C4^{\Delta TEC}$ mice relative to $C4^{WT}$ mice (Fig. 3E). T_{conv} cells in cluster 4 were characterized by high expression of *Cxcr6* and *Ccr2*, low expression of *Tcf7* and *Ccr7*, and adoption of a proliferative profile including expression of *Mki67* (Fig. 3D and fig. S7B), indicative of proliferating T_{conv} cells that had initiated effector cell programs. T_{conv} cells in cluster 6 were also proliferative on the basis of *Mki67* expression but exhibited an inverse expression pattern of other signature genes, including low expression of *Cxcr6* and *Ccr2* and high expression of *Tcf7* and *Ccr7* (Fig. 3D and fig. S7B), and exhibited hallmarks of cycling stemlike central-memory T cells.

C4-specific T_{conv} cells elicited in $C4^{WT}$ and $C4^{\Delta TEC}$ mice expressed comparable amounts of transcripts encoding T helper (T_H) subset–defining transcription factors, including high amounts of the T_H1-associated genes *Tbx21* and *Cxcr3* and low amounts of *Gata3*, *Rorc*, and *Bcl6* (fig. S7C). However, analysis of protein expression by flow cytometry revealed that a larger fraction of MJ23 T_{conv} cells elicited in $C4^{\Delta TEC}$ hosts expressed the T_H1-associated T-bet protein (encoded by *Tbx21*) relative to those elicited in $C4^{WT}$ hosts (fig. S7, D and E). Collectively, these findings suggest that in $C4^{WT}$ mice, C4-specific T_{reg} cells prevent autoimmunity during *Lm[C4]* infection by stifling the proliferative potential and T_H1 skewing of T_{conv} of shared specificity and by restricting the emergence of at least two T_{conv} cell states—those of proliferative effector cells and stemlike central-memory T cells.

We also examined the C4-specific T cell response to *Lm[C4]* challenge using monoclonal

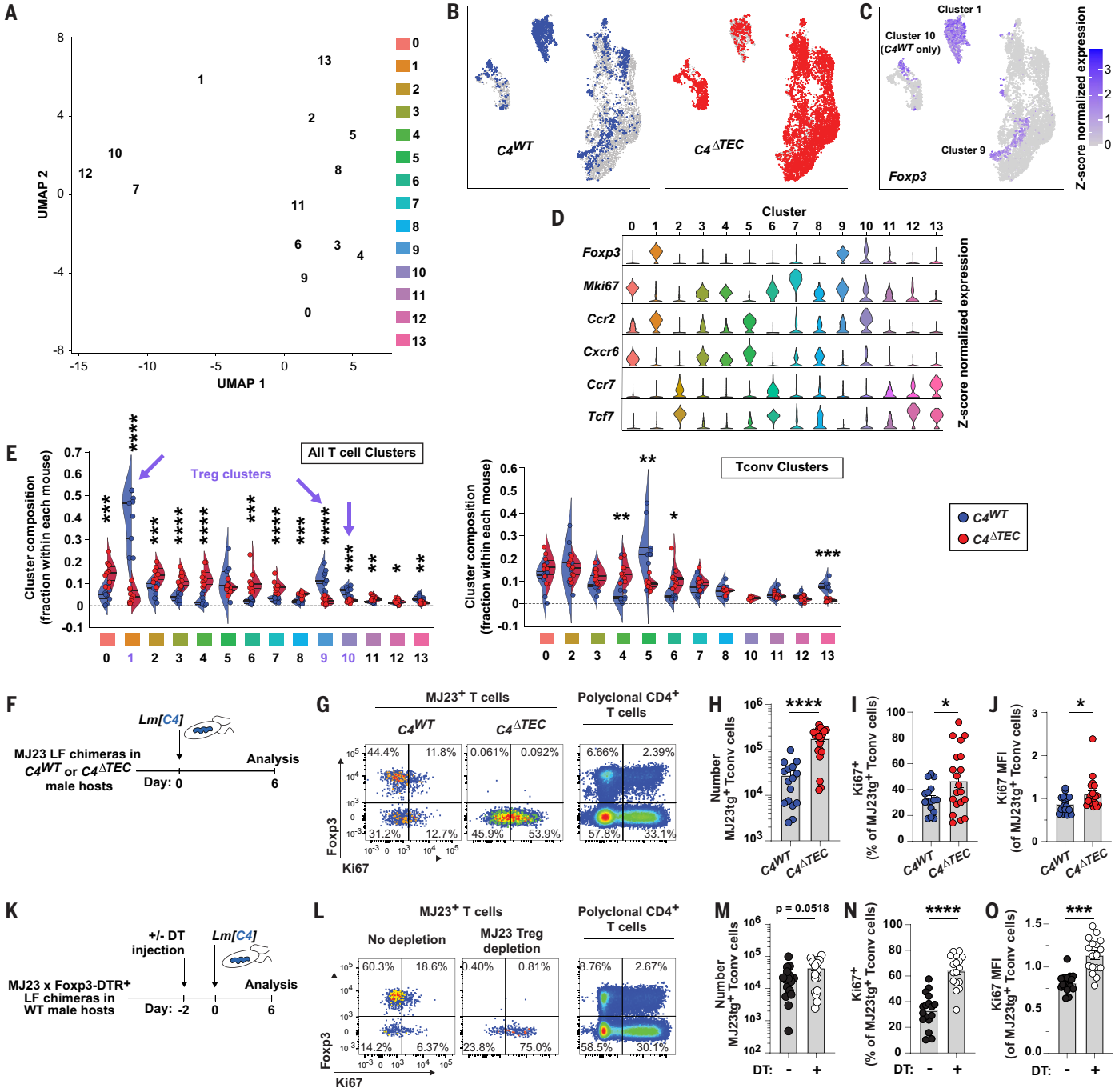

Fig. 3. C4-specific T_{reg} cells restrict the emergence of C4-specific T_{conv} cells exhibiting proliferative and stemlike central-memory states during *Lm[C4]* infection. (**A** to **E**) *C4*^{WT} and *C4*$^{\Delta TEC}$ male mice were challenged intravenously with 10^7 CFU *Lm[C4]* as in Fig. 2C. At 4 days after infection, C4/I-A^b tetramer$^+$ CD4$^+$ T cells were purified by cell sorting from the spleen, and cells from individual mice were tagged, pooled, and subjected to scRNA-seq (10X platform). n = 9, *C4*^{WT}; n = 10, *C4*$^{\Delta TEC}$. (A) Unsupervised clustering and UMAP embedding of scRNA-seq 5′ gene expression data. Clusters 0 to 13 are indicated. (B) UMAP embedding of cells derived from either genotype. A total of 1593 *C4*^{WT}-derived cells and 5246 *C4*$^{\Delta TEC}$-derived cells are depicted. (C) *Z*-score normalized expression of *Foxp3*. Clusters 1, 9, and *C4*^{WT}-derived cells in cluster 10 were designated as T_{reg} cells, while all other cells were T_{conv} cells. (D) Violin plots depicting *z*-score normalized expression of select genes in each cluster. (E) For the *C4*^{WT} and *C4*$^{\Delta TEC}$ settings, fraction of total T cells (left) or T_{conv}-assigned cells (right) in each cluster, relative to the total number of cells from each mouse. (**F**) Experimental schematic for (G) to (J). LF MJ23 chimeric mice were generated in *C4*^{WT} and *C4*$^{\Delta TEC}$ male hosts using MJ23tg$^+$ *Rag1*$^{-/-}$ marrow and challenged with *Lm[C4]*. n = 16, *C4*^{WT}; n = 20, *C4*$^{\Delta TEC}$. (**G**) Representative analysis of Ki67 versus Foxp3 expression by MJ23$^+$ or polyclonal CD4$^+$ T cells isolated from the spleen after *Lm[C4]* infection. Frequency of cells within the gates is denoted. (**H** to **J**) Pooled data from (G) showing the number of MJ23$^+$ CD4$^+$ T_{conv} cells (H), the frequency of Ki67$^+$ cells among MJ23$^+$ CD4$^+$ T cells (I), and the normalized MFI of Ki67 expressed among MJ23$^+$ CD4$^+$ T cells (J). (**K**) Experimental schematic for (L) to (O). LF MJ23 chimeric mice were generated in wild-type male hosts using MJ23tg$^+$ *Rag1*$^{-/-}$ *Foxp3*^{DTR} marrow and challenged with *Lm[C4]*. In the experimental group, host mice were depleted of MJ23 T_{reg} cells 2 days before infection by a single dose of DT. n = 17, no depletion (– DT); n = 17, MJ23 T_{reg} depletion

(+ DT). (**L**) Representative analysis of Ki67 versus Foxp3 expression by MJ23$^+$ or polyclonal CD4$^+$ T cells. The frequency of cells within the gates is denoted. (**M** to **O**) Pooled data from (L) showing the number of MJ23$^+$ CD4$^+$ T_{conv} cells (M), the frequency of Ki67$^+$ cells among MJ23$^+$ CD4$^+$ T_{conv} cells (N), and the mean fluorescence intensity (MFI) of Ki67 on MJ23$^+$ CD4$^+$ T_{conv} cells (O). Flow cytometric gating strategy is described in fig. S13. The *n* values represent the number of mice. Data are pooled from multiple independent experiments: $n = 3$ [(G) to (J)], $n = 4$ [(L) to (O)]. In (A) to (C), each symbol represents one cell. In (E), (H) to (J), and (M) to (O), each symbol represents one mouse. Violin plots in (D) and (E) represent data from pooled mice. Graphs show mean and quartiles (E) or mean ± SEM [(H) to (J) and (M) to (O)]. *P* values were calculated by two-way ANOVA (E) or Welch's *t* test [(H) to (J) and (M) to (O)] (*$P < 0.05$; **$P < 0.01$; ***$P < 0.001$; ****$P < 0.0001$; n.s. = $P > 0.05$).

MJ23 T cells. Given previous work showing that clonal deletion does not affect the thymic selection of MJ23 T cells (*40*), analysis of T_{reg} and T_{conv} cells expressing the fixed MJ23 TCR eliminated the variables of clonal deletion and TCR-pMHC binding properties. We established two distinct scenarios in which the response of MJ23 T_{conv} cells to *Lm[C4]* infection was assessed in the presence or absence of MJ23 T_{reg} cells. In the first setting (Fig. 3, F to J), we analyzed the response in MJ23 BMCs generated in $C4^{WT}$ hosts, which harbored a mixture of MJ23 T_{reg} cells and MJ23 T_{conv} cells at baseline (fig. S1G), and compared this with the response in BMCs generated in $C4^{\Delta TEC}$ hosts, which harbored MJ23 T_{conv} cells but lacked MJ23 T_{reg} cells (fig. S7F). In the second setting (Fig. 3, K to O, and fig. S7, G to J), we generated MJ23 BMCs in $C4^{WT}$ hosts using MJ23tg bone marrow harboring the $Foxp3^{DTR\text{-}EGFP}$ allele, subjected half of these BMCs to selective MJ23 T_{reg} cell depletion through DT administration (fig. S7, G and I), and subsequently challenged with *Lm[C4]*. In both scenarios, the presence of MJ23 T_{reg} cells stifled the proliferative competency of clonally matched MJ23 T_{conv} cells during *Lm[C4]* infection (Fig. 3, F to O), consistent with our above reported findings for polyclonal C4/I-A^b–specific T cells (Fig. 3, D and E).

C4-specific MJ23 T_{reg} cells colocalize with a fraction of MJ23 T_{conv} cells in the lymph node to limit TCR signaling and IL-2 sensing during Lm[C4] *infection*

We hypothesized that C4-specific T_{reg} cells might selectively dampen the proliferative and effector cell states adopted by C4-specific T_{conv} cells by competing for access to self-pMHC and/or IL-2 cytokine in the local environment, thereby restricting sustained T_{conv} cell signal integration (*64*, *65*). We performed quantitative multiplexed imaging of *Lm[C4]*-challenged MJ23 BMCs generated in $C4^{WT}$ and $C4^{\Delta TEC}$ mice (Fig. 4A) to generate high-resolution snapshots of MJ23 T_{conv} cells and locally positioned T_{reg} cells (Fig. 4B). We used PD-1 as a readout of TCR signaling intensity, Ki67 as a measure of proliferative competency, and phospho-STAT5 (pSTAT5) as a readout of IL-2 cytokine signaling and examined the local densities of polyclonal or MJ23 T_{reg} cells within 30 μm of each MJ23 T_{conv} cell. We analyzed the response in the liver-draining portal lymph nodes (Fig. 4, A and B), which drain a major site of *Lm* propagation, and focused on day 3 after *Lm[C4]* challenge, reasoning that the mechanisms orchestrating the divergent outcomes in $C4^{WT}$ and $C4^{\Delta TEC}$ mice would manifest during this early stage of T_{conv} cell priming (Fig. 2, H to J).

We then trained a support vector machine (SVM) to objectively assess how MJ23 T_{conv} cell phenotypes might diverge between $C4^{WT}$ and $C4^{\Delta TEC}$ settings in situ (Fig. 4E). This classification model revealed a decision boundary that accurately separated the two groups on the basis of PD-1 and Ki67 expression, with pSTAT5 expression overlaid for further interpretation. Specifically, 84% of the MJ23 T_{conv} cells in the $C4^{WT}$ setting expressed reduced levels of PD-1, pSTAT5, and Ki67, indicating low-grade signaling and proliferation (Fig. 4E). By contrast, 74% of the MJ23 T_{conv} cells in the $C4^{\Delta TEC}$ setting exceeded this boundary and were classified into one of three distinct subpopulations: D1, D2, or D3 (Fig. 4F). D1 cells exhibited elevated TCR signaling alone; D2 cells displayed enhanced TCR signaling, IL-2 signaling, and Ki67 expression; and D3 cells displayed increased Ki67 expression alone. Notably, 26% of MJ23 T_{conv} cells in $C4^{\Delta TEC}$ hosts fell within the boundary established for $C4^{WT}$ hosts (Fig. 4F), suggesting that these cells were effectively constrained by polyclonal T_{reg} cells of unmatched specificity. These data suggest that in the absence of clonally matched T_{reg} cells, there is a heterogeneous MJ23 T_{conv} cell response to *Lm[C4]* infection, with a fraction of MJ23 T_{conv} cells (D2) exhibiting elevated TCR and IL-2 signal integration.

To assess how this fraction is normally controlled by C4-specific T_{reg} cells, we quantified the spatial relationship between MJ23 T_{conv} and MJ23 T_{reg} cells within the liver-draining LNs of $C4^{WT}$ hosts during *Lm[C4]* infection. In contrast to our observations in the pLNs during homeostatic conditions (Fig. 1J), we observed a nonrandom enrichment of MJ23 T_{reg} cells within microdomains surrounding 37% of MJ23 T_{conv} cells (Fig. 4G). MJ23 T_{reg} cells constituted ~5 to 15% of T_{reg} cells within these microdomains despite representing only ~1% of the global T_{reg} cell pool. These proximal MJ23 T_{reg} cells exhibited elevated expression of PD-1 and pSTAT5 compared with distal MJ23 T_{reg} cells that were not positioned near MJ23 T_{conv} cells, as well as to proximally or distally positioned polyclonal T_{reg} cells (Fig. 4, H and I). These data demonstrate that during *Lm[C4]* infection, MJ23 T_{reg} cells colocalize with a fraction of MJ23 T_{conv} cells and become activated to levels beyond that of other T_{reg} cells in the LN, likely owing to engagement with C4-bearing dendritic cells (DCs).

In the absence of MJ23 T_{reg} cells, a fraction of MJ23 T_{conv} cells escape constraint by polyclonal T_{reg} cells during Lm[C4] *infection*

We performed a holistic, fine-grained analysis on the entire landscape of T_{reg} cells proximally positioned within 30 μm of each MJ23 T_{conv} cell in $C4^{WT}$ and $C4^{\Delta TEC}$ hosts. We linked these T_{reg} cells to their nearest MJ23 T_{conv} cell and performed unsupervised hierarchical clustering on the resulting pairings using eight parameters, including the fluorescence intensity of PD-1, pSTAT5, and Ki67 in both cell types, plus the local densities of polyclonal and MJ23 T_{reg} cells (Fig. 5A). This analysis identified five clusters of T_{reg}-T_{conv} cell pairings (Fig. 5B) that differed in their proportional representations between $C4^{WT}$ and $C4^{\Delta TEC}$ settings (Fig. 5C and fig. S8A) and exhibited clear demarcation when visualized in a low-dimensional embedding of all features using UMAP (fig. S8, B to D). Comparable clusters were also obtained by initially averaging the proximal T_{reg} cell phenotypes and applying the same computational methods outlined above (fig. S9, A to D). Overall, our holistic analysis revealed a range of local T_{reg} cell microenvironments associated with distinct MJ23 T_{conv} cell phenotypes (fig. S8, E to H).

Three of the five clusters exhibited over- or underenrichment in $C4^{WT}$ or $C4^{\Delta TEC}$ hosts with effect sizes greater than twofold that could not be explained by chance (Fig. 5C and tables S1 and S2). Cluster P5 appeared almost exclusively in $C4^{WT}$ conditions (Fig. 5C) and comprised highly activated MJ23 T_{reg} cells and their polyclonal T_{reg} cell neighbors, which were positioned near weakly activated MJ23 T_{conv} cells with low PD-1 and Ki67 (Fig. 5, B to D). Notably, many MJ23 T_{reg} cells expressed elevated amounts of Ki67 when not colocalized with MJ23 T_{conv} cells (fig. S9E). Cluster P1, by contrast, was enriched in $C4^{\Delta TEC}$ mice, comprising ~34% of the T_{reg}-T_{conv} pairings in this setting (Fig. 5C). The MJ23 T_{conv} cells associated with

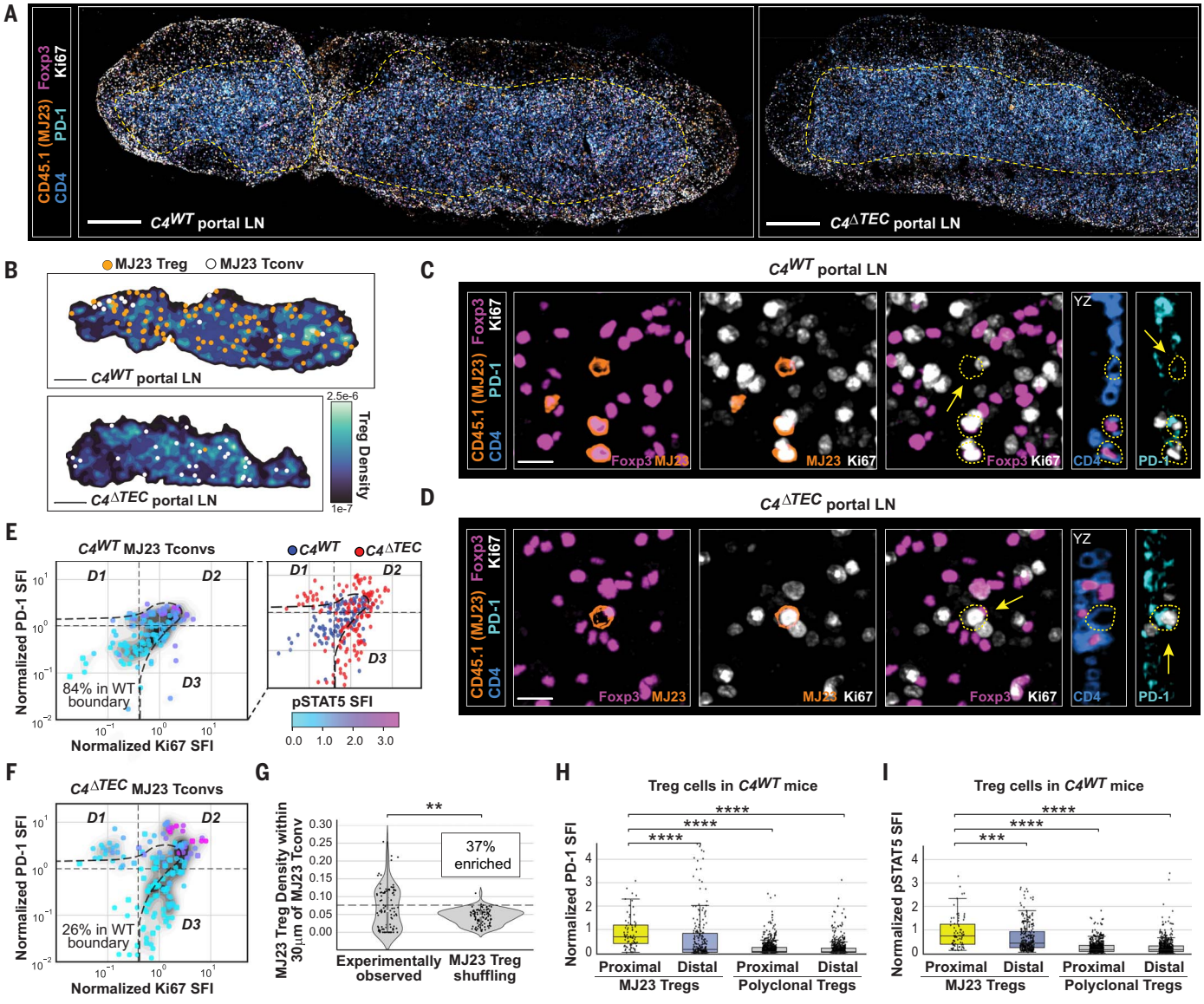

Fig. 4. C4-specific MJ23 T_{reg} cells colocalize with a fraction of MJ23 T_{conv} cells in the lymph node to limit TCR signaling and IL-2 sensing during *Lm[C4]* infection. LF MJ23 chimeric mice were generated in $C4^{WT}$ and $C4^{\Delta TEC}$ male hosts using bone marrow from MJ23 *Rag1*$^{-/-}$ mice. More than six weeks after engraftment, host mice were infected with 10^7 CFU *Lm[C4]*. Three days after *Lm[C4]* challenge, the liver-draining portal LNs were fixed, sectioned, and immunostained, and CD4$^+$ T cells were analyzed by multiplexed confocal microscopy. n = 6, $C4^{WT}$; n = 4, $C4^{\Delta TEC}$, where n denotes number of mice. (**A**) Representative confocal micrographs depicting 20-μm LN sections. Images depict CD45.1, Ki67, Foxp3, CD4, and PD-1 immunostaining. Scale bars: 250 μm. (**B**) Spatial kernel density function of polyclonal T_{reg} cells in the paracortical region of the LNs, depicted as shown in the color scale. The dots depict MJ23 T_{reg} and MJ23 T_{conv} cells. Scale bars: 250 μm. (**C** and **D**) Representative confocal micrographs depicting individual MJ23 T_{reg} and T_{conv} cells and surrounding microenvironments in LNs of $C4^{WT}$ (C) and $C4^{\Delta TEC}$ (D) mice. Dotted yellow circles highlight cells of interest, including MJ23 T_{conv} cells (yellow arrows). MJ23 cells are masked on CD45.1. Scale bars: 15 μm. (**E** and **F**) Pooled data depicting the normalized Ki67, PD-1, and pSTAT5 summed fluorescence intensity (SFI) of MJ23 T_{conv} cells from mice of the two genotypes, with pSTAT5 denoted in the color scale. n = 123, $C4^{WT}$; n = 147, $C4^{\Delta TEC}$. The dashed bold line represents the SVM decision boundary trained to distinguish between $C4^{WT}$ and $C4^{\Delta TEC}$ MJ23 T_{conv} cells on the basis of PD-1 and Ki67 expression [(E), right]. The percentage of MJ23 T_{conv} cells that fall within the $C4^{WT}$ SVM boundary is indicated. KDEs based on MJ23 T_{conv} cell PD-1 and Ki67 expression are depicted (shading). The dashed vertical and horizontal lines depict high and low thresholds for Ki67 and PD-1, respectively. (**G**) Pooled data depicting the observed proximal density of MJ23 T_{reg} cells surrounding MJ23 T_{conv} cells in LNs of $C4^{WT}$ hosts, compared with the density after the positions of MJ23 T_{reg} cells were randomly shuffled across the positions of all polyclonal T_{reg} cells. n = 100, shuffled; n = 100, observed. The percentage of observed data that falls outside the 95% confidence interval of the null model (shuffled condition) is indicated. (**H** and **I**) Pooled data depicting normalized PD-1 (H) and pSTAT5 (I) SFI on MJ23 T_{reg} and polyclonal T_{reg} cells in LNs of $C4^{WT}$ hosts. Proximal cells are those observed within 30 μm of an MJ23 T_{conv} cell. n = 89, proximal MJ23; n = 581, distal MJ23; n = 670, proximal polyclonal; n = 670, distal polyclonal. The n values indicate the number of cells [(E) to (I)]. Data are pooled from two or three independent experiments. Each symbol represents one MJ23 T_{conv} cell [(E) to (G)] or one T_{reg} cell [(H) and (I)]. Mean and quartiles are indicated [(G) to (I)]. P values were calculated by Mann-Whitney test with Bonferroni correction [(H) and (I)] or as described in the Materials and methods (G) (**P < 0.01; ***P < 0.001; ****P < 0.0001).

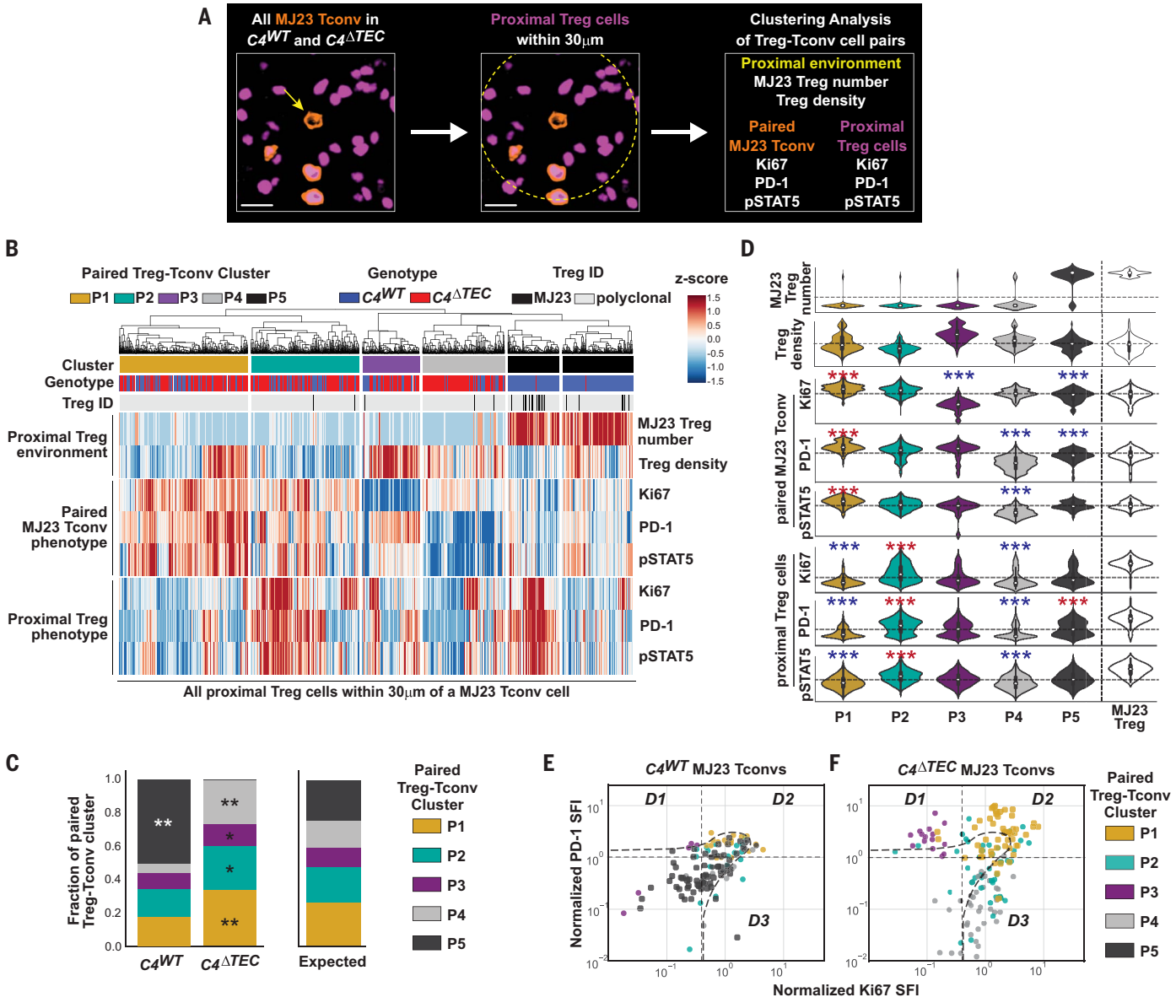

Fig. 5. In the absence of MJ23 T_{reg} cells, a fraction of MJ23 T_{conv} cells escape constraint by polyclonal T_{reg} cells during *Lm[C4]* infection. See Fig. 4 for experimental setup of multiplexed confocal microscopy analysis. n = 6, $C4^{WT}$; n = 4, $C4^{\Delta TEC}$; where n denotes number of mice. (**A**) Schematic for analysis of proximal T_{reg}-T_{conv} cell pairings. Scale bars: 15 μm. (**B**) Heatmap of unsupervised clustering of proximal T_{reg}-T_{conv} cell pairings. n = 75, proximal MJ23 T_{reg} cells; n = 3066, proximal polyclonal T_{reg} cells. T_{reg}-T_{conv} cell pairings were classified into five distinct clusters (P1 to P5). The genotype ($C4^{WT}$ or $C4^{\Delta TEC}$) and T_{reg} cell identity (MJ23 or polyclonal) are indicated. (**C**) Plots showing the proportion of proximal T_{reg}-T_{conv} cell pairings in each cluster as a fraction of the total pairings in mice of either genotype. The rightmost bar plot depicts the frequency of each cluster expected by chance under a random permutation null model (*P < 0.05; **P < 0.05 with an effect size of at least 25% difference from the null model). (**D**) Pooled data showing the $\log_2$-transformed normalized SFI of each parameter for the indicated clusters. Plots are shown for either proximal T_{reg} cells or their paired MJ23 T_{conv} cells. The indicated parameter was compared with the average for all other clusters (***$P < 8.3 \times 10^{-5}$). Plots depicting parameters for MJ23 T_{reg} cells are included (white). Red and blue asterisks indicate parameters that were significantly increased or decreased, respectively. (**E** and **F**) Pooled data depicting the expression of Ki67 versus PD-1 on MJ23 T_{conv} cells from $C4^{WT}$ (E) and $C4^{\Delta TEC}$ (F) mice, as in Fig. 4, E and F. Each symbol represents one MJ23 T_{conv} cell, with the color denoting the most abundant cluster assigned by the proximal T_{reg}-T_{conv} cell pairings in (B). The dashed bold lines represent the SVM decision boundary. The dashed vertical and horizontal lines depict high versus low thresholds for Ki67 and PD-1, respectively. Data are pooled from two or three independent experiments. Mean and quartiles are indicated (D). P values were calculated by Welch's t test with Bonferroni correction (D) or as described in the Materials and methods (C).

this cluster exhibited elevated amounts of PD-1, Ki67, and pSTAT5 compared with MJ23 T_{conv} cells across all other clusters (Fig. 5, B and D). This activation phenotype was associated with weakly activated polyclonal T_{reg} cells, with low and high local densities (Fig. 5, B and D). Thus, a fraction of MJ23 T_{conv} cells received enhanced TCR signaling in the absence of proximal C4-specific T_{reg} cells, likely increasing their ability to sense IL-2 in the local environment and sustain their proliferative burst (*20*, *66*). Cluster P4 was also highly enriched in $C4^{\Delta TEC}$ mice,

comprising ~26% of the T_{reg}-T_{conv} pairings in such mice (Fig. 5C). MJ23 T_{conv} cells associated with this cluster expressed intermediate levels of Ki67 but low amounts of PD-1 and pSTAT5, potentially representing proliferative cells that have terminated TCR and IL-2 signal integration after disengagement from antigen-bearing DCs (*67*–*69*). This T_{conv} cell proliferative phenotype was associated with moderate local densities of polyclonal T_{reg} cells exhibiting negligible TCR and IL-2 signaling (Fig. 5, B and D). Notably, many of the MJ23 T_{conv} cells associated with clusters P1 and P4 mapped to either the D2 or D3 MJ23 T_{conv} cell phenotypes, respectively (Fig. 5F), demonstrating strong concordance between these two orthogonal analyses.

The remaining two clusters of T_{reg}-T_{conv} pairings exhibited statistically significant over- or underenrichment in $C4^{WT}$ or $C4^{\Delta TEC}$ hosts, but with smaller effect sizes. Collectively, our findings suggest that in a setting of elevated self-antigen presentation during bacterial infection, T_{reg} cells form specific microenvironments around individual self-specific T_{conv} cells and attenuate TCR signaling, IL-2 signaling, and proliferative potential to varying degrees. However, although some self-specific T_{conv} cells are constrained sufficiently by polyclonal T_{reg} cells, a subpopulation requires T_{reg} cells of matched specificity to prevent escape. These findings reveal a second tier of T_{reg} cell–mediated control based on local specificity matching that is crucial for preventing autoimmunity in distinct immunological settings.

To understand how C4-specific T_{reg} cells selectively constrain T_{conv} cells of matched specificity without affecting pathogen-specific T_{conv} cells, we engineered attenuated *Lm* expressing the C4 self-peptide linked to a foreign ovalbumin-derived peptide ($OVA_{323\text{-}339}$, OVAp) by protease-sensitive cleavage sites (*Lm[C4+OVAp]*). Expressing C4 and OVAp within the same source protein promotes presentation of the two peptides by the same APC after cleavage in MHC-II–associated processing compartments. Using this system, the activation and positioning of MJ23 T_{reg} and T_{conv} cells can be directly compared to that of TCR transgenic T cells expressing the OVAp-reactive OT-II TCR (OT-II) (*70*) To this end, we generated MJ23 BMCs in $C4^{WT}$ and $C4^{\Delta TEC}$ male hosts, seeded in naïve OT-II T_{conv} cells, challenged mice with *Lm[C4+OVAp]*, and analyzed the response (fig. S10A). The expansion and activation status of OT-II T_{conv} cells was comparable in the $C4^{WT}$ and $C4^{\Delta TEC}$ settings when measured by flow cytometry (fig. S10, B and C) and quantitative imaging (fig. S10, D to H), further demonstrating that MJ23 T_{reg} cells selectively affected the MJ23 T_{conv} cell response without affecting the T_{conv} response to a linked, foreign peptide. Whereas 21% of MJ23 T_{conv} cells were marked by proximally positioned MJ23 T_{reg} cells (fig. S10, I and J), only 9% of OT-II T_{conv} cells were similarly marked (fig. S10K), suggesting that OT-II and MJ23 T_{conv} cells were asymmetrically dispersed within the lymph nodes. Consistent with this, only a small fraction of OT-II T_{conv} cells exhibited nonrandom colocalization with MJ23 T_{conv} cells (7 or 8%) (fig. S10, J and K). Additionally, we found that MJ23 T_{reg} cells elicited after *Lm[C4+OVAp]* challenge displayed elevated amounts of the $I\text{-}A^b$ MHC-II molecule relative to polyclonal T_{reg} cells within the same samples (fig. S11, A to C), suggesting either elevated expression of MHC-II by MJ23 T_{reg} cells and/or acquisition of cognate C4/$I\text{-}A^b$ complexes from antigen-bearing APCs through trogocytosis, which has been proposed as a potential mechanism by which T_{reg} cells can selectively regulate T_{conv} cells of shared nonself pMHC-II specificity (*33*). Thus, OT-II T_{conv} cells and MJ23 T cells were differentially distributed within the lymph node paracortex and were likely engaging distinct antigen-bearing APCs at this early time point. This spatial separation might explain why the presence of MJ23 T_{reg} cells had no impact on the OT-II T_{conv} cell response to the linked foreign peptide.

C4-specific MJ23 T_{reg} cells are intrinsically poised to accumulate earlier than clonally matched T_{conv} cells during Lm[C4] *infection*

Our imaging data suggest that during *Lm[C4]* infection, MJ23 T_{reg} cells compete with MJ23 T_{conv} cells for self-pMHC and IL-2–dependent signals. Consistent with this enhanced signaling, the majority of MJ23 T_{reg} cells expressed Ki67 at day 3 after *Lm[C4]* challenge (fig. S9E), indicating active division. We therefore hypothesized that MJ23 T_{reg} cells might proliferate earlier or more extensively than MJ23 T_{conv} cells in the early stages of the response, endowing MJ23 T_{reg} cells with an intrinsic competitive advantage over their T_{conv} counterparts. To test this idea, we generated MJ23 BMCs in $C4^{WT}$ and $C4^{\Delta TEC}$ male hosts, challenged mice with *Lm[C4]*, and analyzed the MJ23 T cell response in this early period (Fig. 6A and fig. S12A). In $C4^{WT}$ hosts, a major fraction of both MJ23 T_{reg} cells and T_{conv} cells expressed high densities of Ki67 by day 2 after *Lm[C4]* challenge (fig. S12,

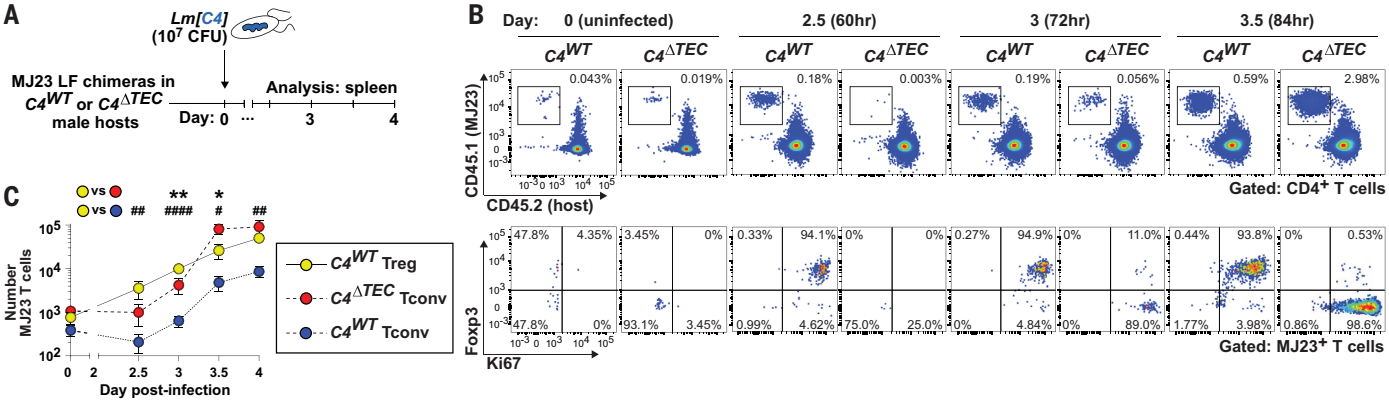

Fig. 6. C4-specific MJ23 T_{reg} cells are intrinsically poised to accumulate earlier than clonally matched T_{conv} cells during *Lm[C4]* infection. (**A**) Experimental schematic. LF MJ23 chimeric mice were generated in $C4^{WT}$ and $C4^{\Delta TEC}$ male hosts using $MJ23tg^{+}$ $Rag1^{-/-}$ marrow and challenged with *Lm[C4]*. *n* = 7, $C4^{WT}$ d0; *n* = 8, $C4^{\Delta TEC}$ d0; *n* = 6, $C4^{WT}$ d2.5; *n* = 6, $C4^{\Delta TEC}$ d2.5; *n* = 11, $C4^{WT}$ d3; *n* = 12, $C4^{\Delta TEC}$ d3; *n* = 6, $C4^{WT}$ d3.5; *n* = 6, $C4^{\Delta TEC}$ d3.5; *n* = 6, $C4^{WT}$ d4; *n* = 8, $C4^{\Delta TEC}$ d4. (**B**) Representative flow cytometric analysis of $CD4^{+}$ T cells (top) and Ki67 versus Foxp3 expression by $MJ23^{+}$ $CD4^{+}$ T cells isolated from the spleen (bottom). In the top row, MJ23 T cells fall within the $CD45.1^{+}CD45.2^{neg}$ gate. The frequency of cells within the gates is denoted. (**C**) Pooled data from (B) showing the number of $MJ23^{+}$ $CD4^{+}$ T_{reg} and T_{conv} cells recovered at the indicated time points. Asterisk symbols denote comparison of $C4^{WT}$ T_{reg} to $C4^{\Delta TEC}$ T_{conv}, and hashtag symbols denote comparison of $C4^{WT}$ T_{reg} to $C4^{WT}$ T_{conv}. Flow cytometric gating strategy is described in fig. S13. The *n* values represent the number of mice. Data are pooled from three to five independent experiments. Each symbol represents the mean ± SEM of pooled mice (C). *P* values were calculated by two-tailed nonparametric Mann-Whitney test (*$P < 0.05$; **$P < 0.01$; ****$P < 0.0001$).

B to E). Despite this, MJ23 T_{reg} cell expansion occurred earlier than that of MJ23 T_{conv} cells in $C4^{WT}$ hosts, preceding MJ23 T_{conv} expansion by 12 hours or more (Fig. 6B). As a result, MJ23 T_{reg} cells outnumbered MJ23 T_{conv} cells by >15-fold from days 2.5 to 4 (Fig. 6C). Notably, the pro-proliferative high-affinity IL-2 receptor alpha chain, CD25, was uniformly expressed by MJ23 T_{reg} cells but not T_{conv} cells at day 2 (fig. S12F). A similar delay in MJ23 T_{conv} cell expansion was also observed in *Lm[C4]*-challenged $C4^{\Delta TEC}$ hosts lacking MJ23 T_{reg} cells (Fig. 6, B and C), suggesting that this proliferation lag was an intrinsic feature of the MJ23 T_{conv} cell response, irrespective of the presence or absence of MJ23 T_{reg} cells. Despite this delay, MJ23 T_{conv} cells expanded markedly in $C4^{\Delta TEC}$ hosts by later time points (day 3.5 and beyond) (Fig. 6C and fig. S12G), consistent with previous studies of T_{conv} cells reactive to pathogen-expressed nonself peptides (*71*, *72*). No differences were observed in the number of polyclonal T_{reg} or T_{conv} cells between $C4^{WT}$ and $C4^{\Delta TEC}$ hosts (fig. S12H). Thus, these data indicate that C4-specific MJ23 T_{reg} cells are intrinsically poised to accumulate more rapidly after *Lm[C4]* challenge relative to T_{conv} cells expressing the same TCR.

Discussion

Through the study of $CD4^+$ T cells reactive to a natural self-pMHC antigen, our work revealed that T_{reg} cells of matched specificity were not required for the control of self-pMHC–specific T_{conv} cells at steady state but were crucial for the control of such T_{conv} cells activated by elevated self-peptide presentation during infection. When elevated self-peptide was available, nonspecific bystander tolerance mechanisms and T_{reg} cells reactive to other self-pMHCs were unable to prevent autoimmunity. This second tier of regulation by antigen-matched T_{reg} cells may be especially relevant for immunological insults that are proposed drivers of autoimmunity, including pathogen-associated epitope mimicry or the release of self-antigens and inflammatory signals triggered by infection-induced cell death. Importantly, T_{reg} cell–mediated control of T_{conv} cells of shared self-specificity had no impact on the T_{conv} cell response to pathogen-derived nonself peptides. These findings support a T_{reg} cell–centric model of self-nonself discrimination in which the immune system generates T_{reg} cells reactive to highly antigenic self-pMHC ligands, selectively focusing immunosuppression on T_{conv} cells of matched specificity during strong immunological challenges. This model differs from, and complements, classical paradigms of self-nonself discrimination based on clonal inactivation or deletion of self-reactive T cells.

Our work also revealed cellular mechanisms underpinning the nature of pMHC-specific T_{reg}-mediated suppression. First, the finding that C4-specific T_{reg} cells were intrinsically poised to expand earlier than T_{conv} cells expressing the same TCR reveals a feature of T_{reg} cells that may boost T_{reg} cell numbers at sites of antigen presentation (*20*). Second, C4-specific T_{reg} cells did not prevent antigen recognition and initial activation of C4-specific T_{conv} cells elicited by *Lm[C4]* challenge but instead stifled the proliferative competency and differentiation of these cells, thereby preventing their infiltration into the target organ. Third, the MJ23 T_{conv} cell response elicited by *Lm[C4]* infection in the absence of MJ23 T_{reg} cells exhibited considerable heterogeneity; many MJ23 T_{conv} cells adopted an attenuated phenotype indicative of constraint, whereas others displayed hallmarks of strong activation. These findings suggest that T_{reg} cells of matched self-specificity are required to control a minor fraction of C4-specific T_{conv} cells that would otherwise escape control by polyclonal T_{reg} cells and other modes of tolerance. On the basis of previously defined principles of T_{reg} cell motility and function, we hypothesize that self-specific T_{reg} cells make serial short-term liaisons with antigen-bearing DCs (*73*, *74*), thereby transiently disrupting sustained TCR signaling by T_{conv} cells of matched self-specificity through direct competition for access to cognate self-pMHCs or selective removal of self-pMHC ligands from APCs through trogocytosis (*33*). Lastly, our data demonstrated that within a setting associated with widespread innate activation and elevated self-antigen presentation, C4-specific T_{reg} cells controlled T_{conv} cell responses to C4 without affecting T_{conv} cell responses to a pathogen-derived peptide, thereby enforcing self-nonself discrimination. Given these divergent outcomes, future studies will be needed to understand how pathogen-specific T_{conv} cells avoid constraint by T_{reg} cells of shared specificity during infection. We hypothesize that this effect may be driven in part by the relative T_{reg}/T_{conv} cell ratios of the antigen-specific T cell pool; $CD4^+$ T cells reactive to foreign peptides are generally characterized by a low percentage of T_{reg} cells (*27*, *32*), whereas T cells reactive to defined T_{reg}-selecting self-peptides are marked by a predominant fraction of T_{reg} cells (*27*, *28*, *39*).

Materials and methods

Mice

The following mice were purchased from the Jackson Laboratory and bred and maintained at the University of Chicago: C57BL/6J (B6) mice, $CD45^{-1/1}$ B6.SJL-$Ptprc^a$ $Pepc^b$/BoyJ mice, $Rag1^{-/-}$ B6.129S7-$Rag1^{tm1Mom}$/J mice, $Aire^{-/-}$ B6.129S2-$Aire^{tm1.1Doi}$/J mice, $Foxp3^{DTR\text{-}eGFP}$ B6.129(Cg)-$Foxp3^{tm3(DTR/GFP)Ayr}$/J mice, $Foxn1^{Cre}$ B6(Cg)-$Foxn1^{tm3(cre)Nrm}$/J mice, and OT-IItg B6.Cg-Tg($TcraTcrb$)^{425Cbn}/J mice. MJ23tg $Rag1^{-/-}$ $CD45^{-1/1}$ mice were generated as described previously (*38*). All mice were generated on a pure B6 background or were fully backcrossed to the B6 background. All mice were initially bred and maintained under specific pathogen–free conditions in accordance with the animal care and use regulations of the University of Chicago, Association for Assessment and Accreditation of Laboratory Animal Care Unit #001020, Public Health Service Policy on Humane Care and Use of Laboratory Animals policy assurance #D16-00322 (A3523-01), and United States Department of Agriculture registration #33-R0151. All experimental procedures were approved by the Institutional Animal Care and Use Committee at the University of Chicago. OT-IItg GFP^+ mice were bred from Tg(CAG-EGFP)D4Nagy/J mice and B6.129S6-$Rag2^{tm1Fwa}$ Tg($TcraTcrb$)425Cbn mice, which were purchased from the Jackson Laboratory and obtained from the NIAID-Taconic exchange program, respectively, and maintained at the NIAID in accordance with the procedures outlined in the NIH Guide for the Care and Use of Laboratory Animals. Prior to infection with *L. monocytogenes*, experimental mice were transferred to an isolated ABSL-2 facility. Where applicable, infected mice were housed in separate cages from uninfected littermates. Mice were housed in sterile and ventilated microisolation cages, up to five mice per cage, and fed irradiated standard pellet chow and reverse osmosis water ad libitum in a 12-hour light/dark cycle, with room temperature at 22° ± 1°C. All cages contained sterile quarter-inch corncob bedding and a nestlet for environmental enrichment. Mice were euthanized by 5 min of CO_2 asphyxiation followed by cervical dislocation, following approved guidelines. Mice for experiments were age-matched, littermates when possible and where indicated, and assigned to experimental groups based on genotype. All BMC mice used in this study were 6 to 10 weeks old at the time of irradiation and reconstitution and 12 to 16 weeks old at the time of experimental treatment or analysis. All non-BMC mice were 8 to 12 weeks old at the time of experimental treatment.

Generation of low-frequency MJ23tg chimeric mice

Bone marrow cells from $MJ23tg^+$ $Rag1^{-/-}$ $CD45^{-1/1}$ $Foxp3^{DTR/Y}$ mice were T cell–depleted using CD90.2 MACS MicroBeads (Miltenyi Biotec) and following the manufacturer's protocol. A mixture consisting of 20% $MJ23tg^+$ bone marrow and 80% B6 filler bone marrow was prepared, and 5×10^6 cells were retro-orbitally injected into sublethally (500 rads) irradiated host mice. Mice were used for experiments >6 weeks after engraftment.

Diphtheria-toxin mediated depletion of MJ23tg and polyclonal T_{reg} cells

Diphtheria toxin (Sigma) was reconstituted at 5 μg/ml in sterile molecular grade water following manufacturer's protocol and stored at

−80°C before use. Diphtheria toxin aliquots were frozen and thawed once. A single injection of 1 μg of diphtheria toxin was administered intraperitoneally to deplete MJ23tg T_{reg} cells, either 3 days before analysis of uninfected chimeric mice or 2 days before *Lm* challenge of chimeric mice. To transiently deplete polyclonal T_{reg} cells in *Foxp3*$^{DTR\text{-}eGFP}$ mice, a total of three 1-μg injections of diphtheria toxin were administered on days −1, 0, and 2 of infection, where day 0 is the day of infection.

Immunofluorescence confocal microscopy of lymph node sections

Sample preparation

Mice were sacrificed, and lymph nodes were immediately and carefully isolated and placed in RPMI 1640 medium supplemented with 10% fetal bovine serum (FBS) and 1X penicillin-streptomycin [pen/strep (R10)] on ice. Lymph nodes (LNs) were trimmed of fat using a stereo dissection microscope and fine forceps and fixed for 16 to 20 hours at 4°C with agitation in BD Cytoperm/Cytofix (BD Bioscience) diluted to 1% paraformaldehyde in phosphate-buffered saline (PBS). LNs were subsequently washed three times in PBS for 10 min per wash with agitation at 4°C and stored overnight on ice. The next day, LNs were further trimmed of remaining fat and dehydrated for 24 hours in a 30% sucrose solution made in 0.1 M phosphate buffer. LNs were then embedded in optimal cutting temperature (O.C.T.) compound (Sakura Finetek), frozen on dry ice, and stored at −80°C. Sagittal LN sections measuring 18 to 50 μm were prepared using a cryostat (Leica) equipped with a Surgipath DB80LX blade (Leica). Cryochamber and specimen cooling was set to −17°C.

Immunofluorescence staining and image acquisition

Tissue sections were adhered to Superfrost Plus microscopy slides (VWR), permeabilized using 0.1% Triton X-100 for 10 min at 22°C, blocked in 5% mouse serum for 1 hour at 22°C, and washed in PBS. Tissue sections were next incubated with directly conjugated primary antibodies diluted in PBS for 15 hours at 4°C. After washing three times in PBS for 10 min per wash at 22°C, samples were mounted in Fluoromount-G (SouthernBiotech), which was allowed to cure for a minimum of 14 hours at 22°C. All imaging was performed using No. 1.5 coverglass (VWR). For pStat5 immunostaining, fixed tissue sections were permeabilized in prechilled 100% methanol for 18 min at −20°C, washed extensively in PBS, blocked in 5% donkey serum for 1 hour at 22°C, and washed further in PBS. Tissue sections were next incubated with unconjugated anti-pSTAT5 (C11C5) diluted in PBS for 15 hours at 4°C. Following washing in PBS at 22°C, tissue sections were incubated with fluor-conjugated donkey anti-rabbit F(ab')$_2$ fragments (Jackson ImmunoResearch Laboratories) for 2 hours at 22°C. Sections were then washed four times in PBS for 10 min per wash at 22°C before mounting in Fluoromount-G as described above. Digital images were acquired using the following systems: (i) an upright or inverted Leica TCS SP8 X (Leica) equipped with a pulsed white light laser, four Gallium-Arsenide Phosphide Hybrid Detectors, one photomultiplier tube, and a 40× [numerical aperture (NA) = 1.3] oil immersion objective lens; or (ii) an inverted Leica Stellaris 8 equipped with a pulsed white light laser, Power HyD S, X, and R detectors set to analog mode, and a 40× (NA = 1.25) glycerol objective lens. For tissue sections, images were acquired with a lateral pixel size of 0.271 to 0.286 μm, an axial step size of 1 μm, and detector bit-depth of 12. Image acquisition was controlled using LAS X software.

For experiments using *Lm[C4-OVAp]* (figs. S10 and S11), the Brilliant Stain Buffer polymer block was added into the blocking solution to reduce background. Spectrally overlapping fluorophores were simultaneously used for staining sections to achieve more extensive multiplexing. Spectral spillover was corrected through linear unmixing as previously described (*75*), with some modifications. To reduce the number of required staining controls, subsets of fluorophores with negligible spectral overlap were used to stain each control sample. To obtain compensation matrices for unmixing, average pixel intensities inside regions of interest with specific signal were first measured using the Channel Dye Separation module of LAS X. Then, spillover coefficients were calculated for channels where spectral spillover was expected. Unmixing was performed on raw images using a custom-built Imaris XTension, linked in the GitHub (*76*).

Image processing and segmentation

Image files generated in LAS X software were converted into ".ims" files in Imaris software (Bitplane) and subjected to a 1 pixel Gaussian filter on all channels to reduce noise. Owing to high background after infection, the PD-1 channel was subjected to an additional baseline subtraction and 2x2x2 median filter. Image segmentation was performed in Imaris using the "Surface Object Creation" module, which employs a seeded region growing, *k*-means, and watershed algorithm to define individual cells of interest. To create surfaces on nuclear molecules, the following parameters were used: surface detail = 0.3, background subtraction = 7 μm, seed points = 3.2 μm, voxel filter > 100. To create surfaces on membrane molecules, the following parameters were used: surface detail = 0.3, background subtraction = 14 μm, seed points = 6.8 μm, voxel filter > 100. Polyclonal T_{reg} cells were segmented using Foxp3. MJ23 T_{reg} cells were initially segmented using Foxp3 and refined using Foxp3 and CD4 filters. MJ23 T_{conv} cells were initially segmented using CD45.1 and refined using Foxp3 and CD4 filters. PD-1$^+$ polyclonal T_{conv} cells were identified by creating artificial nuclei using the CD4 channel and Fiji (*20*) and using PD-1 and Foxp3 filters. In all cases, segmentation artifacts were excluded using volume and nonspecific staining thresholds. Each MJ23 T_{reg}, MJ23 T_{conv}, and PD-1$^+$ polyclonal T_{conv} cell was manually reviewed and corrected when necessary. For images depicting MJ23 T_{reg} and T_{conv} cells, the CD45.1 fluorescence was masked in Imaris to improve visual clarity.

Quantitative image and spatial analysis

Processing and normalization

Surface objects for MJ23 T_{conv} cells, MJ23 T_{reg} cells, polyclonal T_{conv} cells, and polyclonal T_{reg} cells were exported as .csv files from Imaris with spatial coordinates and fluorescence intensity (FI) values of each target protein. These files were then imported into Python for downstream analysis. To enable accurate comparisons across samples, the FI values of each target protein on each cell per imaging day were normalized to the average FI value of the target protein across all MJ23 T_{conv} cells in *C4*^{WT} settings acquired on the same day. Cells with artificially high FI values due to segmentation errors or noise, here designated as 100 times the average FI of a given target protein, were removed. Additionally, duplicated MJ23 T_{reg} and T_{conv} cells were removed from the segmented polyclonal T_{reg} and T_{conv} cell objects, respectively. Lastly, batch effects for FI values were corrected across samples using the Harmony algorithm (*77*, *78*).

Density computation and statistics

To further account for technical variation across different tissue sections, experiments, and mice, we developed a standardized metric for quantifying and comparing T_{reg} cell densities. Average T_{reg} cell density of a given lymph node tissue section was determined by (i) enumerating T_{reg} cells within the entire tissue section, (ii) finding the semiminor and semimajor axes in the *xy* plane and the height of the tissue section in the *z* plane, (iii) computing the volume of the elliptic cylinder, (iv) performing a two-dimensional kernel density estimate (KDE) on the entire tissue section to remove regions with artificially low cell densities, thereby yielding the effective tissue volume, and (v) dividing the total number of T_{reg} cells by this effective volume to calculate a standardized average T_{reg} cell density. The local polyclonal T_{reg} cell densities around specific T_{conv} cells were then found by (i) enumerating T_{reg} cells within 30 μm of the specific T_{conv} cell, (ii) computing the volume of the local 30-μm cylinder, and (iii) dividing the number of local T_{reg} cells by this volume.

To quantitatively assess the enrichment of these standardized local T_{reg} cell densities around MJ23 T_{conv} cells, we generated spatial permutation null models by randomly shuffling the labels of each cell type across their fixed positional coordinates. The densities around each MJ23 T_{conv} cell were averaged over 499 permutations and plotted for visual aid. An empirical *P* value was then determined by calculating the proportion of permutations in which the averaged local T_{reg} cell densities around the MJ23 T_{conv} cells were greater than or equal to the observed distribution and then dividing these selected permutations by the total number of permutations.

Clustering and statistics

Unless otherwise stated, statistical comparisons between target protein FI values on cells were conducted using the Mann-Whitney *U* test with the Bonferroni correction. The SVM to classify MJ23 T_{conv} cells from $C4^{WT}$ and $C4^{\Delta TEC}$ mice was trained on all MJ23 T_{conv} cell Ki67 and PD-1 expression data. Various train-test splits and regularization schemes did not affect the decision boundary learned from the data (not shown). The final SVM boundary used in the manuscript was implemented with sklearn's SVC function with the radial basis function kernel and gamma=0.7. Hierarchical clustering of the proximal T_{reg}-T_{conv} cell pairs was implemented in R with the pheatmap function using the UPGMA (unweighted pair group method with arithmetic mean) linkage method on the correlation metric. The normalized FI value of each target protein on both the T_{reg}-T_{conv} cell pairs were $\log_2$ transformed and then further transformed into *z*-scores on the basis of the target protein's range for all T_{conv}-T_{reg} cell pairs (i.e., across the rows) before hierarchical clustering. The "local MJ23 T_{reg} number" was set to −0.5 for all T_{reg} cells from the $C4^{\Delta TEC}$ genotype to account for the near-global loss of MJ23 T_{reg} cells throughout the host. Importantly, our hierarchical clustering results exhibited only modest differences without this global bias, with a small subset of the activated MJ23 T_{reg} cells now mapping to cluster P3 instead of cluster P5 (data not shown). To identity the most dominant cluster identity of MJ23 T_{conv} cells, we calculated the majority vote of the local T_{reg}-T_{conv} pair cluster identities, resulting in a single cluster identity for the local environment. Welch's *t* test with the Bonferroni correction was used to statistically compare the FI values of identified clusters for a given cell type against the average respective FI value of all other clusters. A permutation test was used to determine statistical significance of the observed cluster proportions within $C4^{WT}$ or $C4^{\Delta TEC}$ hosts compared with the null model where the genotype labels were randomly distributed across samples.

MJ23 and OT-II T_{conv} cell transfers

Splenocytes derived from MJ23tg$^+$ *Rag1*$^{-/-}$ CD45$^{.1/.1}$ mice were isolated into a single-cell suspension in RPMI 1640 medium supplemented with 10% FBS and 1X pen/strep (R10) using a 70-μm filter and enriched for CD4$^+$ T cells using MACS (Miltenyi Biotec) following the manufacturer's protocol. MJ23$^+$ CD4$^+$ T cells do not develop into Foxp3$^+$ T_{reg} cells in MJ23tg$^+$ *Rag1*$^{-/-}$ mice owing to niche overload (*38*) and are therefore T_{conv} cells. The indicated number of enriched MJ23 T_{conv} cells were injected retro-orbitally into male hosts and identified at the indicated time point as CD45.1$^+$ CD4$^+$ T cells. In some experiments, splenocytes were isolated and transferred from MJ23tg$^+$ *Rag1*$^{-/-}$ CD45$^{.1/.2}$ mice and identified as CD45.1$^+$ CD45.2$^+$ CD4$^+$ T cells. For OT-II T_{conv} transfers, splenocytes were similarly isolated from OT-IItg$^+$ *Rag1*$^{-/-}$ CD45$^{.1/.1}$ mice (for experiments analyzed by flow cytometry) or OT-IItg$^+$ *Rag2*$^{-/-}$ *Ubc*-GFP$^{+/+}$ mice (for experiments analyzed by quantitative imaging). The indicated number of enriched OT-II T_{conv} cells were injected retro-orbitally into male hosts and identified at the indicated time point as CD45.1$^+$ CD4$^+$ T cells (by flow cytometry) or GFP$^+$ CD4$^+$ T cells (by quantitative imaging).

Generation of $C4^{\Delta TEC}$ mice

Tcaf3(exon5)^{floxed} mice were generated by CRISPR-Cas9–mediated insertion following the *Easi*-CRISPR method described in (*79*). Guide sites targeting the introns immediately upstream and downstream of exon 5 of the *Tcaf3* locus were designed using the IDT design tool and were templated from the antisense strand. A 595–base pair (bp) single-stranded ODN Megamer (IDT) templated from the sense strand was used to replace the region between the guide cut sites; it was designed to span the entire exon 5 region and included two unidirectional *loxP* sites at each guide cut site with 68 bp and 80 bp homology arms upstream and downstream of the respective *loxP* inserts: 5′-AAATATGAATACTCTTCTGGGAGGTCTGAAAGGAGACAGGGAAAGACAACGGAGATTTATTACCAAGCATAACTTCGTATAATGTATGCTATACGAAGTTATTATCTTTTCATGTGGTCTACAGTTGAAGGTCTACAATTGAAATCTAGAAAAAAAAAAATGTTGTGGGCCAAGCTAGGTAACTTTTATTTCCAGGTAAGACGACCCAGGAGGAATGGAAGAATCTTATCACACACAGCAAAGCTCCGTGGGGAGAACTAGCCACAGACAATATCATCCTGACAATTCCAACGGTAAACCTCAAGGAGCTTCAGGACCCCTATCCACTGCTCCAACTCTGGGACAAGATGGTAAGGGCTGTAGCCAAGCTGGCAGCCCGGCCCTTCCCTTTTCAGAGAGCTGAGAGGGTCGTACTTGACAAGCAGATTTCATTCGGTAGGTACTTCGTGGGAATGTTCTGAGAGTTGACTTTCCATCCACCTATAACTTCGTATAATGTATGCTATACGAAGTTATGACATAATTTGATGGAGATCAGCTGGGGAAGCCACATCTTTTAAATCTCAAATATACAAAGAGTTACAGGATAGTAAGAC-3′. Alt-R CRISPR-Cas9 crRNA, tracrRNA, and Cas9 nuclease were purchased from IDT. The following sequences were used for crRNA: 5′- GACCACATGAAAAGATAGCT-3′ (upstream) and 5′-CTCCATCAAATTATGTCAGG-3′ (downstream). For microinjections, gRNA was assembled with crRNA and tracrRNA at a 1:2 molar ratio by annealing rampdown from 95°C to 25°C at 5°C/min. gRNAs were subsequently complexed with Cas9 in separate reactions at 250 ng/μl gRNA and Cas9 for 15 min at room temperature. Final injection mix was created at 50 ng/μl each gRNA/Cas9 complex and 10 ng/μl ssODN Megamer and spun at 21,000*g* for 5 min before injection. Mixes were injected into the nuclei of C57BL/6J embryos. Successful integrations were determined by PCR using three primer sets designed to generate products that span the upstream *loxP* site only (5′-CCACTTAACTTCATCCCAGACA-3′ and 5′-CAGAGTTGGAGCAGTGGATAG-3′), the downstream *loxP* site only (5′-CGACCCAGGAGGAATGGA-3′ and 5′-GGAAACTAGCTGGGATAGAGAA-3′), and the entire inserted region out beyond the homology arms (5′-GATCTGGCTTGAGAGAAAGCA-3′ and 5′-GGCAGACTTTGCTTTTCAGT-3′), and was verified by Sanger sequencing. *Tcaf3(exon5)*^{floxed} founder mice were crossed with C57BL/6J mice for two generations, and progeny were subsequently intercrossed with mice of the same founder line and *Foxn1*^{Cre} mice to generate $C4^{\Delta TEC}$ [*Tcaf3(exon5)*$^{flox/flox}$ *Foxn1*-Cre$^+$] mice and $C4^{WT}$ [*Tcaf3(exon5)*$^{flox/flox}$ *Foxn1*-Cre^{neg}] littermate controls. Because *Foxn1* is expressed in the male gametes (*80*), only *Foxn1*-Cre$^+$ females were used for breeding. Proper genotype and Cre-mediated excision were confirmed for each mouse using both a generic Cre primer set (5′-TTACCGGTCGATGCAACGAGT-3′ and 5′-TTCCATGAGTGAACGAACCTGG-3′) and the primer set spanning the entire inserted region of *Tcaf3(exon5)* beyond the homology arms.

CFA immunization

Mice were given a single subcutaneous injection in the flank of 100 μg peptide (GenScript) in 100 μl complete Freund's adjuvant (CFA) emulsion (InvivoGen). CFA emulsion consisted of a 1:1 ratio peptide:CFA. Mice were analyzed 14 days later.

I-A^b tetramer acquisition and production

Tetramers were obtained from the NIH Tetramer Core Facility or produced in-house as previously described (*81*). For tetramers made in-house, C4/I-A^b monomers bearing the $Tcaf3_{646–658}$(648Y) peptide (THYKAPWGELATD) and F1/I-A^b monomers bearing the $Tcaf3_{88-107}$ peptide (CPGAPIAVHSSLASLVNILG) were produced as in (*40*) using *Drosophila* S2 cells and linking the peptide sequence to the N terminus of the β-chain. For tetramers obtained from the NIH Tetramer Core Facility, C4/I-A^b monomers bearing the $Tcaf3_{646–658}$(648Y) peptide (THYKAPWGELATD),

F1/I-A^b monomers bearing the truncated Tcaf3$_{90\text{-}106}$ core peptide (GAPIAVHSSLASLVNIL), and LLO/I-A^b monomers bearing the Listeriolysin O$_{190\text{-}201}$ peptide (NEKYAQAYPNVS) were received from the core facility. Tetramers were formed from biotinylated monomers in-house by mixing peptide/I-A^b monomers with streptavidin-APC (PJ27S; Agilent) or streptavidin-phycoerythrin (PE) (PJRS34; Agilent) at a 10% molar excess to biotin-binding sites on the monomers.

I-A^b tetramer staining and enrichment

Tetramer staining was adapted from (*82*). After cell isolation from SLOs or tissue, cells were treated with dasatinib (Sigma) at a final concentration of 50 nM for 30 min at 37°C in minimal staining buffer (PBS with 0.1% NaN_3, 2% normal rat serum, and 2% normal mouse serum, all from Jackson ImmunoResearch, and 10 μg/ml 2.4G2 antibody). PE- or APC-labeled tetramers were added directly to dasatinib-treated cells in minimal staining buffer (without washing) at a final concentration of 100 nM (C4/I-A^b and F1/I-A^b) or 10 nM (LLO/I-A^b) for 1 hour at room temperature. In experiments analyzing tetramer$^+$ cells at individual SLOs or in the prostate, cells were washed and incubated with unconjugated mouse anti-PE antibody (clone PE001; BioLegend) and mouse anti-APC antibody (clone APC003; BioLegend) at a concentration of 10 μg/ml for 20 min at 4°C in minimal staining buffer. The cells were subsequently washed and stained and analyzed by flow cytometry as described below. In peptide/CFA immunization experiments in which SLOs (spleen, inguinal LN, axillary LN, cervical LN, brachial LN, portal LN, para-aortic LN) were pooled, CD4$^+$ cells were enriched before tetramer staining using CD4$^+$ T cell negative selection kit (Miltenyi Biotec) following the manufacturer's protocol. After tetramer staining, cells were enriched through the following method adapted from (*83*): Cells were treated with EasySep PE/APC Positive Selection Kit II (STEMCELL Technologies) per the manufacturer's protocol, with slight modification (25 μl/ml each anti-PE/APC for 15 min at room temperature in minimal staining buffer, followed by 50 μl/ml dextran microbeads without wash for 3 min at room temperature), and enriched using a column-free magnet. The resulting bound fraction was stained and analyzed by flow cytometry as described below.

Genetic engineering of L. monocytogenes

All *L. monocytogenes* strains were engineered using the pPL6-myc shuttle vector as described in (*52*), with modifications in some strains as follows. The peptide or protein of interest to be expressed in *L. monocytogenes* was codon-optimized for expression in *L. monocytogenes* (GenScript), and the coding sequence was synthesized and inserted into the pUC18 vector immediately flanked by BamHI restriction sites (GenScript). Coding sequence fragments were amplified with a Phusion PCR (NEB) using M13 universal forward and reverse primers (IDT) and gel-purified (Qiagen) per the manufacturer's protocol. Amplified fragments and pPL6-myc vector (Freitag Lab) were digested with 1 μl BamHI in Cutsmart buffer (NEB) for 1 hour @ 37°C, gel-purified, and ligated with 1 μl T4 ligase in ligation buffer (NEB) overnight @ 16°C using a 1:6 vector:fragment molar ratio. DH5-alpha *Escherichia coli* were heat-transformed using the ligation reaction mix per the manufacturer's protocol (NEB), and transformed colonies were selected on LB agar plates (Sigma) containing 25 μg/ml chloramphenicol (CAM) (Sigma) overnight @ 37°C. DNA from selected colonies was purified by Miniprep (Qiagen) using the manufacturer's protocol, and sequence integration and directionality were confirmed by Sanger sequencing using the pPL6-Myc_Seq primer (5′-TATTCCTATCTTAAAGTTACTTTTATGTGGAGGC-3′). Correctly integrated plasmids were subsequently transformed into electrocompetent SM10 *E. coli* (Freitag Lab) by electroporation using a Gene-pulser and 0.1 cm Gene-pulser cuvettes (Biorad) and the following settings: capacitance, 25 μF; resistance, 200 ohms; and voltage, 1.8 kV. Electroporated SM10 were selected overnight in LB broth (Gibco) with 25 μg/ml CAM at 37°C shaking, subsequently incubated overnight on LB agar plates with 25 μg CAM @ 37°C, and selected colonies were expanded. Shuttle vector was introduced and stably integrated into *L. monocytogenes* genome through conjugation with SM10. Transformed SM10 and *L. monocytogenes* parent strains (*Lm[parent]*) were grown to lawns overnight at 37°C on agar plates under the following conditions: LB agar with 25 μg/ml CAM and BHI agar (Difco) with 200 μg/ml streptomycin (Strep), respectively. The next day, SM10 was replated in ~1-inch square on fresh antibiotic-free BHI agar plates, *Lm[parent]* was replated directly on top of SM10, and conjugation proceeded for 4 hours at 37°C. After incubation, conjugation mix was selected overnight at 37°C shaking in BHI broth (Difco) containing 7.5 μg/ml CAM and 200 μg strep. Cultures were further selected overnight at 37°C on BHI agar plates (BD) containing 7.5 μg/ml CAM and 200 μg strep. Colonies were isolated, expanded, and stored as 15% glycerol stocks at −80°C. Stable integration was subsequently confirmed by sequencing and using cellular assays.

The final engineered *Lm* strains expressed peptides with the following amino acid sequences: *Lm[C4]*, THSKAPWGELATD; *Lm[F1]*, GAPIAVHSSLASLVNIL; and *Lm[C4+OVAp]*, THSKAPWGELATDGSGMSMDMNGSGISQAVHAAHAEINEAGR. The *Lm[C4+OVAp]* peptide consisted of the C4 peptide and OVA$_{323\text{-}339}$ peptides on the N and C terminal ends, respectively, separated by GSG linkers and an intervening cathepsin cleavage site derived from residues of the mouse Invariant chain which flank the C terminus of the CLIP peptide (MSMDMN).

Infection with L. monocytogenes

L. monocytogenes strains used in this study are described in (*52*). Attenuated strains were derived from the 10403S *prfA(G155S)* Δ*actA* parent strain (NF-L974 in reference). Non-attenuated strains were derived from the 10403S *actA gus plcB prfA(G155S)* parent strain (NF-L943 in reference). The day before infection, glycerol stock of the infecting strain was scraped, dropped in starter culture, and grown overnight at 37°C shaking (225 rpm) in BHI broth (Difco) under CAM (Sigma) selection (7.5 μg/ml). On the day of infection, starter culture was diluted 1:20 in BHI and CAM and grown under analogous conditions and expanded to experimentally determined logarithmic growth phase (~3 hours). Culture was removed and placed on ice for a minimum of 30 min to stall growth. Optical density (OD$_{600}$) of culture was measured and concentration was calculated using the following experimentally determined equation: For attenuated strains, $\log_{10}$[CFU/ml] = 0.6245 (OD$_{600}$) + 8.707; for non-attenuated strains, $\log_{10}$[CFU/ml] = 0.3134(OD$_{600}$) + 8.585. Culture was diluted in PBS inoculum to the desired concentration, and mice were infected intravenously with 10^7 CFU (attenuated strains) or 5×10^3 CFU (non-attenuated strains) in 400 μl. To confirm infecting dose, after the infection, limiting dilutions of inoculum were plated on antibiotic-free BHI agar plates (Difco) and grown overnight at 37°C, and CFUs were quantified the next day.

Cell isolation and flow cytometry

Cells from SLOs were isolated into a single-cell suspension in RPMI 1640 medium supplemented with 10% FBS and 1X pen/strep (R10) using a 70-μm filter. To harvest prostatic lymphocytes, prostates were isolated from the genitourinary tract by microdissection, injected, and digested with Liberase TL (10 mg/ml; Roche) and DNase (20 mg/ml; Roche) in RPMI 1640 medium for 30 min at 37°C. Digested tissue was mechanically disrupted with frosted microscope slides, and viable lymphocytes were enriched using Histopaque 1119 (Sigma). All antibodies used were from BioLegend, eBioscience, BD Biosciences, R&D Systems, or Cell Signaling. Cells were stained with conjugated antibodies specific for the following proteins (with clone name in parentheses): CD4 (GK1.5), CD8β (Ly-3), CD3 (17A2), TCRβ (H57- 597), CD45.1 (A20), CD45.2 (104), CD69 (H1.2F3), Egr2 (erongr2), Ki67 (SolA15), Foxp3 (FJK-16s), CXCR6 (SA051D1), CCR2 (475301), TCF-1 (C63D9), B220 (RA3-6B2), CD11b (M1/70), CD11c (N418), F4/80 (BM8), FR4 (12A5), CD73 (TY/11.8), CD25 (PC61), rabbit IgG anti-Myc (D84C12), and anti-rabbit IgG (polyclonal, Invitrogen). For chemokine receptors CXCR6 and CCR2, cells were stained for 30 min at room

temperature in PBS with 2% FCS before staining for other surface markers. For surface markers, cells were stained for 20 min at 4°C in staining buffer (PBS with 2% FCS, 0.1% NaN_3, 5% normal rat serum, 5% normal mouse serum, and 5% normal rabbit serum, with all sera from Jackson ImmunoResearch, and 10 μg/ml 2.4G2 antibody). In experiments involving tetramer staining, cells were instead stained for 20 min at 4°C in minimal staining buffer (described above). Intracellular staining for Egr2, Ki67, Foxp3, TCF-1, and Myc was performed using fixation and permeabilization buffers (eBioscience) with an overnight antibody incubation at 4°C. In experiments involving Myc staining, a secondary stain was performed the next morning using AF647-conjugated anti-rabbit IgG for 1 hour at 4°C in permeabilization buffer (eBioscience). For infected samples, cell isolation, staining, and fixation was performed in a designated BSL-2 safety cabinet. Flow cytometry was performed on an LSRFortessa (BD Biosciences), and data were analyzed using FlowJo v10.1 software (Tree Star). When reporting protein expression as the percentage of a cell population, samples containing fewer than five cells were excluded from pooled data. Summary plots were created and associated statistics were calculated using GraphPad v10 (Prism).

Single-cell RNA/TCR sequencing of C4/I-A^b tetramer$^+$ cells

Cell isolation and library preparation

To maximize cell viability, cell isolation, staining, enrichment, and fluorescence-activated cell sorting (FACS) was performed over a 12-hour period directly before sequencing, and cells were kept cold or on ice whenever possible. Cells were isolated from the spleens of infected mice, as described above, in two "batches": the first consisting of four $C4^{WT}$ and five $C4^{\Delta TEC}$ mice, and the second consisting of five $C4^{WT}$ and five $C4^{\Delta TEC}$ mice. For each batch, individual spleens were first enriched for $CD4^+$ T cells using $CD4^+$ T cell negative selection kit (Miltenyi Biotec) per the manufacturer's protocol. Individual samples were subsequently stained with C4/I-A^b tetramers as described above. After tetramer staining, individual samples were incubated with anti-PE and anti-APC microbeads (Miltenyi Biotec) for 15 min on ice (100 μl each antibody cocktail per milliliter), washed, and enriched over an autoMACS magnetic column. After enrichment, the individual bound fractions were stained with separate surface marker antibody master mixes, as described above, in minimal staining buffer. Each surface stain master mix contained uniform surface markers common to all mixes but contained 1 of 10 Totalseq-C030X hashing antibodies used to identify cells derived from each mouse. After surface staining, all samples within a batch were pooled, and C4/I-A^b tetramer$^+$ cells were sorted by FACS using a BD FACSAria Fusion 5-18 cytometer. Ultimately, two sorted samples (one per batch) containing C4/I-A^b tetramer$^+$ cells from pooled and hashtagged mice resulted after isolation. These samples were resuspended in 45 μl of sequencing buffer (0.04% BSA in PBS), and 40 μl of each sample was loaded into one of two lanes of a sequencing chip and then subjected to Drop-seq (10X Genomics) to coencapsulate individual cells in reverse emulsion droplets in oil together with one uniquely barcoded mRNA-capture bead. Libraries were derived from single cells then subjected to next-generation sequencing.

10X scRNA-seq quantification

Gene expression matrices for single cells were obtained from raw reads of RNA-seq and feature barcode libraries quantified using CellRanger count v4.0.2 (10X Genomics). TCR sequences for single cells were obtained using CellRanger vdj v.4.0.2 (10X Genomics). Individual samples were further demultiplexed on the basis of feature barcodes, which were used to mark original samples out of the 9 or 10 samples combined in each capture. The maximum feature expression was determined for each cell, and the original sample identity was assigned accordingly, as long as the maximum feature expression constituted at least 80% of the total feature exzpression for that cell. Otherwise, the cell was discarded. TCR sequences were matched to gene expression tables on the basis of shared cell barcodes.

Clustering

All samples from both captures were analyzed together for clustering analysis in the Seurat package in R (*84*). Percent mitochondrial expression was quantified, and cells with >15% mitochondrial expression, <750 genes expressed, or <2000 total unique molecular identifier counts were removed. Gene expression was normalized using NormalizeData() in Seurat, and the top 5000 variable features were identified using FindVariableFeatures(), both with default parameters. Variable features were *z*-scored, and principal components analysis (PCA) was run. JackStraw *P* values and PCA heatmaps were computed to determine the informativeness of each principal component, and the top 45 were selected as features for clustering. Clustering was performed using the Louvain algorithm at resolutions of 0.25, 0.5, 0.75, and 1. Cell types per cluster were determined by comparing the expression level of specific marker genes in those clusters, as well as looking at the percent of cells expressing a functional TCR. On the basis of these comparisons, a final resolution of 1 was retained for further analysis. Two non–T cell clusters were further removed from the analysis. Dimensionality reduction was performed by UMAP to visualize cells and clusters.

Differential gene expression

Cluster-specific genes were identified using differential expression statistics (area under the curve test) between cell clusters using FindAllMarkers() in Seurat with default settings. Differential expression between genotypes was computed using Wilcox test with the FindMarkers() function within each cluster, in turn, in each case setting logfc.threshold to 0 to test all genes and using the false discovery rate correction to adjust *P* values for multiple testing.

Treatment with anti-CD40, LPS, or poly I:C

Mice were treated with a single injection of either *InVivo*Plus anti-mouse CD40 (clone FGK4.5, BioXCell), *InVivo*Plus rat IgG2a Isotype mAb (clone 2A3, BioXCell), *E. coli*–deriver LPS (Sigma), or poly I:C (Sigma). Each agent was administered in 200 μl of corresponding solvent as follows: 100 μg anti-mouse CD40 or isotype antibody intraperitoneally, 5 μg LPS intravenously, 20 μg poly I:C intravenously.

REFERENCES AND NOTES

1. D. Nemazee, Receptor selection in B and T lymphocytes. *Annu. Rev. Immunol.* **18**, 19–51 (2000). doi: 10.1146/annurev.immunol.18.1.19; pmid: 10837051
2. L. Klein, B. Kyewski, P. M. Allen, K. A. Hogquist, Positive and negative selection of the T cell repertoire: What thymocytes see (and don't see). *Nat. Rev. Immunol.* **14**, 377–391 (2014). doi: 10.1038/nri3667; pmid: 24830344
3. D. Mathis, C. Benoist, Aire. *Annu. Rev. Immunol.* **27**, 287–312 (2009). doi: 10.1146/annurev.immunol.25.022106.141532; pmid: 19302042
4. B. Kyewski, L. Klein, A central role for central tolerance. *Annu. Rev. Immunol.* **24**, 571–606 (2006). doi: 10.1146/annurev.immunol.23.021704.115601; pmid: 16551260
5. W. Yu *et al*., Clonal deletion prunes but does not eliminate self-specific αβ $CD8^+$ T lymphocytes. *Immunity* **42**, 929–941 (2015). doi: 10.1016/j.immuni.2015.05.001; pmid: 25992863
6. J. Yan, M. J. Mamula, Autoreactive T cells revealed in the normal repertoire: Escape from negative selection and peripheral tolerance. *J. Immunol.* **168**, 3188–3194 (2002). doi: 10.4049/jimmunol.168.7.3188; pmid: 11907071
7. R. T. Taniguchi *et al*., Detection of an autoreactive T-cell population within the polyclonal repertoire that undergoes distinct autoimmune regulator (Aire)-mediated selection. *Proc. Natl. Acad. Sci. U.S.A.* **109**, 7847–7852 (2012). doi: 10.1073/pnas.1120607109; pmid: 22552229
8. V. Lee *et al*., The endogenous repertoire harbors self-reactive $CD4^+$ T cell clones that adopt a follicular helper T cell-like phenotype at steady state. *Nat. Immunol.* **24**, 487–500 (2023). doi: 10.1038/s41590-023-01425-0; pmid: 36759711
9. C. Bouneaud, P. Kourilsky, P. Bousso, Impact of negative selection on the T cell repertoire reactive to a self-peptide: A large fraction of T cell clones escapes clonal deletion. *Immunity* **13**, 829–840 (2000). doi: 10.1016/S1074-7613(00)00080-7; pmid: 11163198
10. L. A. Kalekar *et al*., $CD4^+$ T cell anergy prevents autoimmunity and generates regulatory T cell precursors. *Nat. Immunol.* **17**, 304–314 (2016). doi: 10.1038/ni.3331; pmid: 26829766
11. P. A. Savage, D. E. J. Klawon, C. H. Miller, Regulatory T cell development. *Annu. Rev. Immunol.* **38**, 421–453 (2020). doi: 10.1146/annurev-immunol-100219-020937; pmid: 31990619
12. J. M. Kim, J. P. Rasmussen, A. Y. Rudensky, Regulatory T cells prevent catastrophic autoimmunity throughout the lifespan of mice. *Nat. Immunol.* **8**, 191–197 (2007). doi: 10.1038/ni1428; pmid: 17136045
13. S. Z. Josefowicz, L. F. Lu, A. Y. Rudensky, Regulatory T cells: Mechanisms of differentiation and function. *Annu. Rev. Immunol.* **30**, 531–564 (2012). doi: 10.1146/annurev.immunol.25.022106.141623; pmid: 22224781
14. E. M. Shevach, Mechanisms of $Foxp3^+$ T regulatory cell-mediated suppression. *Immunity* **30**, 636–645 (2009). doi: 10.1016/j.immuni.2009.04.010; pmid: 19464986
15. P. Pandiyan, L. Zheng, S. Ishihara, J. Reed, M. J. Lenardo, $CD4^+CD25^+Foxp3^+$ regulatory T cells induce cytokine deprivation–mediated apoptosis of effector $CD4^+$ T cells. *Nat. Immunol.* **8**, 1353–1362 (2007). doi: 10.1038/ni1536; pmid: 17982458

16. K. Wing *et al*., CTA-4 control over Foxp3$^+$ regulatory T cell function. *Science* **322**, 271–275 (2008). doi: 10.1126/science.1160062; pmid: 18845758
17. H. von Boehmer, Mechanisms of suppression by suppressor T cells. *Nat. Immunol.* **6**, 338–344 (2005). doi: 10.1038/ni1180; pmid: 15785759
18. Y. P. Rubtsov *et al*., Regulatory T cell-derived interleukin-10 limits inflammation at environmental interfaces. *Immunity* **28**, 546–558 (2008). doi: 10.1016/j.immuni.2008.02.017; pmid: 18387831
19. Z. Liu *et al*., Immune homeostasis enforced by co-localized effector and regulatory T cells. *Nature* **528**, 225–230 (2015). doi: 10.1038/nature16169; pmid: 26605524
20. H. S. Wong *et al*., A local regulatory T cell feedback circuit maintains immune homeostasis by pruning self-activated T cells. *Cell* **184**, 3981–3997.e22 (2021). doi: 10.1016/j.cell.2021.05.028; pmid: 34157301
21. M. F. Cusick, J. E. Libbey, R. S. Fujinami, Molecular mimicry as a mechanism of autoimmune disease. *Clin. Rev. Allergy Immunol.* **42**, 102–111 (2012). doi: 10.1007/s12016-011-8294-7; pmid: 22095454
22. M. Rojas *et al*., Molecular mimicry and autoimmunity. *J. Autoimmun.* **95**, 100–123 (2018). doi: 10.1016/j.jaut.2018.10.012; pmid: 30509385
23. X. Yang *et al*., Autoimmunity-associated T cell receptors recognize HLA-B*27-bound peptides. *Nature* **612**, 771–777 (2022). doi: 10.1038/s41586-022-05501-7; pmid: 36477533
24. O. S. Qureshi *et al*., Trans-endocytosis of CD80 and CD86: A molecular basis for the cell-extrinsic function of CTLA-4. *Science* **332**, 600–603 (2011). doi: 10.1126/science.1202947; pmid: 21474713
25. C. Oderup, L. Cederbom, A. Makowska, C. M. Cilio, F. Ivars, Cytotoxic T lymphocyte antigen-4-dependent down-modulation of costimulatory molecules on dendritic cells in CD4$^+$ CD25$^+$ regulatory T-cell-mediated suppression. *Immunology* **118**, 240–249 (2006). doi: 10.1111/j.1365-2567.2006.02362.x; pmid: 16771859
26. S. Malchow *et al*., Aire enforces immune tolerance by directing autoreactive T cells into the regulatory T cell lineage. *Immunity* **44**, 1102–1113 (2016). doi: 10.1016/j.immuni.2016.02.009; pmid: 27130899
27. D. Malhotra *et al*., Tolerance is established in polyclonal CD4$^+$ T cells by distinct mechanisms, according to self-peptide expression patterns. *Nat. Immunol.* **17**, 187–195 (2016). doi: 10.1038/ni.3327; pmid: 26726812
28. T. Hassler *et al*., Inventories of naive and tolerant mouse CD4 T cell repertoires reveal a hierarchy of deleted and diverted T cell receptors. *Proc. Natl. Acad. Sci. U.S.A.* **116**, 18537–18543 (2019). doi: 10.1073/pnas.1907615116; pmid: 31451631
29. B. D. Stadinski *et al*., A temporal thymic selection switch and ligand binding kinetics constrain neonatal Foxp3$^+$ T_{reg} cell development. *Nat. Immunol.* **20**, 1046–1058 (2019). doi: 10.1038/s41590-019-0414-1; pmid: 31209405
30. A. Spence *et al*., Revealing the specificity of regulatory T cells in murine autoimmune diabetes. *Proc. Natl. Acad. Sci. U.S.A.* **115**, 5265–5270 (2018). doi: 10.1073/pnas.1715590115; pmid: 29712852
31. E. Kieback *et al*., Thymus-derived regulatory T cells are positively selected on natural self-antigen through cognate interactions of high functional avidity. *Immunity* **44**, 1114–1126 (2016). doi: 10.1016/j.immuni.2016.04.018; pmid: 27192577
32. L. F. Su, D. Del Alcazar, E. Stelekati, E. J. Wherry, M. M. Davis, Antigen exposure shapes the ratio between antigen-specific Tregs and conventional T cells in human peripheral blood. *Proc. Natl. Acad. Sci. U.S.A.* **113**, E6192–E6198 (2016). doi: 10.1073/pnas.1611723113; pmid: 27681619
33. B. Akkaya *et al*., Regulatory T cells mediate specific suppression by depleting peptide–MHC class II from dendritic cells. *Nat. Immunol.* **20**, 218–231 (2019). doi: 10.1038/s41590-018-0280-2; pmid: 30643268
34. Q. Tang *et al*., Visualizing regulatory T cell control of autoimmune responses in nonobese diabetic mice. *Nat. Immunol.* **7**, 83–92 (2006). doi: 10.1038/ni1289; pmid: 16311599
35. M. Xu *et al*., c-MAF-dependent regulatory T cells mediate immunological tolerance to a gut pathobiont. *Nature* **554**, 373–377 (2018). doi: 10.1038/nature25500; pmid: 29414937
36. Y. Y. Setiady *et al*., Physiologic self antigens rapidly capacitate autoimmune disease-specific polyclonal CD4$^+$CD25$^+$ regulatory T cells. *Blood* **107**, 1056–1062 (2006). doi: 10.1182/blood-2005-08-3088; pmid: 16223778
37. J. Meng *et al*., Testosterone regulates tight junction proteins and influences prostatic autoimmune responses. *Horm. Cancer* **2**, 145–156 (2011). doi: 10.1007/s12672-010-0063-1; pmid: 21761342
38. S. Malchow *et al*., Aire-dependent thymic development of tumor-associated regulatory T cells. *Science* **339**, 1219–1224 (2013). doi: 10.1126/science.1233913; pmid: 23471412
39. J. D. Leonard *et al*., Identification of natural regulatory T cell epitopes reveals convergence on a dominant autoantigen. *Immunity* **47**, 107–117.e8 (2017). doi: 10.1016/; j.immuni.2017.06.015; pmid: 28709804
40. D. E. J. Klawon *et al*., Altered selection on a single self-ligand promotes susceptibility to organ-specific T cell infiltration. *J. Exp. Med.* **218**, e20200701 (2021). doi: 10.1084/jem.20200701; pmid: 33914024
41. J. E. Harris *et al*., Early growth response gene-2, a zinc-finger transcription factor, is required for full induction of clonal anergy in CD4$^+$ T cells. *J. Immunol.* **173**, 7331–7338 (2004). doi: 10.4049/jimmunol.173.12.7331; pmid: 15585857
42. I. Miller *et al*., Ki67 is a graded rather than a binary marker of proliferation versus quiescence. *Cell Rep.* **24**, 1105–1112.e5 (2018). doi: 10.1016/j.celrep.2018.06.110; pmid: 30067968
43. H. S. Wong, R. N. Germain, Robust control of the adaptive immune system. *Semin. Immunol.* **36**, 17–27 (2018). doi: 10.1016/j.smim.2017.12.009; pmid: 29290544
44. J. C. Vahl *et al*., Continuous T cell receptor signals maintain a functional regulatory T cell pool. *Immunity* **41**, 722–736 (2014). doi: 10.1016/j.immuni.2014.10.012; pmid: 25464853
45. A. G. Levine, A. Arvey, W. Jin, A. Y. Rudensky, Continuous requirement for the TCR in regulatory T cell function. *Nat. Immunol.* **15**, 1070–1078 (2014). doi: 10.1038/ni.3004; pmid: 25263123
46. J. Gordon *et al*., Specific expression of lacZ and cre recombinase in fetal thymic epithelial cells by multiplex gene targeting at the *Foxn1* locus. *BMC Dev. Biol.* **7**, 69 (2007). doi: 10.1186/1471-213X-7-69; pmid: 17577402
47. M. Hamon, H. Bierne, P. Cossart, *Listeria monocytogenes*: A multifaceted model. *Nat. Rev. Microbiol.* **4**, 423–434 (2006). doi: 10.1038/nrmicro1413; pmid: 16710323
48. P. Lauer, M. Y. Chow, M. J. Loessner, D. A. Portnoy, R. Calendar, Construction, characterization, and use of two *Listeria monocytogenes* site-specific phage integration vectors. *J. Bacteriol.* **184**, 4177–4186 (2002). doi: 10.1128/JB.184.15.4177-4186.2002; pmid: 12107135
49. K. J. Mueller, N. E. Freitag, Pleiotropic enhancement of bacterial pathogenesis resulting from the constitutive activation of the *Listeria monocytogenes* regulatory factor PrfA. *Infect. Immun.* **73**, 1917–1926 (2005). doi: 10.1128/IAI.73.4.1917-1926.2005; pmid: 15784531
50. D. A. Portnoy, V. Auerbuch, I. J. Glomski, The cell biology of *Listeria monocytogenes* infection: The intersection of bacterial pathogenesis and cell-mediated immunity. *J. Cell Biol.* **158**, 409–414 (2002). doi: 10.1083/jcb.200205009; pmid: 12163465
51. L. M. Shetron-Rama *et al*., Isolation of *Listeria monocytogenes* mutants with high-level *in vitro* expression of host cytosol-induced gene products. *Mol. Microbiol.* **48**, 1537–1551 (2003). doi: 10.1046/j.1365-2958.2003.03534.x; pmid: 12791137
52. L. Yan *et al*., Selected *prfA** mutations in recombinant attenuated *Listeria monocytogenes* strains augment expression of foreign immunogens and enhance vaccine-elicited humoral and cellular immune responses. *Infect. Immun.* **76**, 3439–3450 (2008). doi: 10.1128/IAI.00245-08; pmid: 18474644
53. J. A. Vázquez-Boland *et al*., *Listeria* pathogenesis and molecular virulence determinants. *Clin. Microbiol. Rev.* **14**, 584–640 (2001). doi: 10.1128/CMR.14.3.584-640.2001; pmid: 11432815
54. J. M. Blander, R. Medzhitov, Toll-dependent selection of microbial antigens for presentation by dendritic cells. *Nature* **440**, 808–812 (2006). doi: 10.1038/nature04596; pmid: 16489357
55. J. G. Cyster, Chemokines, sphingosine-1-phosphate, and cell migration in secondary lymphoid organs. *Annu. Rev. Immunol.* **23**, 127–159 (2005). doi: 10.1146/annurev.immunol.23.021704.115628; pmid: 15771568
56. P. D. Krueger, K. C. Osum, M. K. Jenkins, CD4$^+$ memory T-cell formation during type 1 immune responses. *Cold Spring Harb. Perspect. Biol.* **13**, a038141 (2021). doi: 10.1101/cshperspect.a038141; pmid: 33903156
57. G. Escobar, D. Mangani, A. C. Anderson, T cell factor 1: A master regulator of the T cell response in disease. *Sci. Immunol.* **5**, eabb9726 (2020). doi: 10.1126/sciimmunol.abb9726; pmid: 33158974
58. I. Siddiqui *et al*., Intratumoral Tcf1$^+$PD-1$^+$CD8$^+$ T cells with stem-like properties promote tumor control in response to vaccination and checkpoint blockade immunotherapy. *Immunity* **50**, 195–211.e10 (2019). doi: 10.1016/j.immuni.2018.12.021; pmid: 30635237
59. S. A. Nish *et al*., CD4$^+$ T cell effector commitment coupled to self-renewal by asymmetric cell divisions. *J. Exp. Med.* **214**, 39–47 (2017). doi: 10.1084/jem.20161046; pmid: 27923906
60. B. C. Miller *et al*., Subsets of exhausted CD8$^+$ T cells differentially mediate tumor control and respond to checkpoint blockade. *Nat. Immunol.* **20**, 326–336 (2019). doi: 10.1038/s41590-019-0312-6; pmid: 30778252
61. S. V. Gearty *et al*., An autoimmune stem-like CD8 T cell population drives type 1 diabetes. *Nature* **602**, 156–161 (2022). doi: 10.1038/s41586-021-04248-x; pmid: 34847567
62. D. Zou *et al*., CD4$^+$ T cell immunity is dependent on an intrinsic stem-like program. *Nat. Immunol.* **25**, 66–76 (2024). doi: 10.1038/s41590-023-01682-z; pmid: 38168955
63. Y. Xia *et al*., BCL6-dependent TCF-1$^+$ progenitor cells maintain effector and helper CD4$^+$ T cell responses to persistent antigen. *Immunity* **55**, 1200–1215.e6 (2022). doi: 10.1016/j.immuni.2022.05.003; pmid: 35637103
64. K. A. Allison *et al*., Affinity and dose of TCR engagement yield proportional enhancer and gene activity in CD4+ T cells. *eLife* **5**, e10134 (2016). doi: 10.7554/eLife.10134; pmid: 27376549
65. W. Liao, J. X. Lin, W. J. Leonard, IL-2 family cytokines: New insights into the complex roles of IL-2 as a broad regulator of T helper cell differentiation. *Curr. Opin. Immunol.* **23**, 598–604 (2011). doi: 10.1016/j.coi.2011.08.003; pmid: 21889323
66. R. A. Gottschalk *et al*., Distinct influences of peptide-MHC quality and quantity on in vivo T-cell responses. *Proc. Natl. Acad. Sci. U.S.A.* **109**, 881–886 (2012). doi: 10.1073/pnas.1119763109; pmid: 22223661
67. B. B. Au-Yeung *et al*., A sharp T-cell antigen receptor signaling threshold for T-cell proliferation. *Proc. Natl. Acad. Sci. U.S.A.* **111**, E3679–E3688 (2014). doi: 10.1073/pnas.1413726111; pmid: 25136127
68. A. Bohineust, Z. Garcia, H. Beuneu, F. Lemaître, P. Bousso, Termination of T cell priming relies on a phase of unresponsiveness promoting disengagement from APCs and T cell division. *J. Exp. Med.* **215**, 1481–1492 (2018). doi: 10.1084/jem.20171708; pmid: 29588347
69. H. D. Moreau, P. Bousso, Visualizing how T cells collect activation signals in vivo. *Curr. Opin. Immunol.* **26**, 56–62 (2014). doi: 10.1016/j.coi.2013.10.013; pmid: 24556401
70. M. J. Barnden, J. Allison, W. R. Heath, F. R. Carbone, Defective TCR expression in transgenic mice constructed using cDNA-based alpha- and beta-chain genes under the control of heterologous regulatory elements. *Immunol. Cell Biol.* **76**, 34–40 (1998). doi: 10.1046/j.1440-1711.1998.00709.x; pmid: 9553774
71. J. Quiel *et al*., Antigen-stimulated CD4 T-cell expansion is inversely and log-linearly related to precursor number. *Proc. Natl. Acad. Sci. U.S.A.* **108**, 3312–3317 (2011). doi: 10.1073/pnas.1018525108; pmid: 21292989
72. J. K. Whitmire, N. Benning, J. L. Whitton, Precursor frequency, nonlinear proliferation, and functional maturation of virus-specific CD4$^+$ T cells. *J. Immunol.* **176**, 3028–3036 (2006). doi: 10.4049/jimmunol.176.5.3028; pmid: 16493061
73. F. Marangoni *et al*., Expansion of tumor-associated Treg cells upon disruption of a CTLA-4-dependent feedback loop. *Cell* **184**, 3998–4015.e19 (2021). doi: 10.1016/j.cell.2021.05.027; pmid: 34157302
74. M. P. Matheu *et al*., Imaging regulatory T cell dynamics and CTLA4-mediated suppression of T cell priming. *Nat. Commun.* **6**, 6219 (2015). doi: 10.1038/ncomms7219; pmid: 25653051
75. M. Y. Gerner, W. Kastenmuller, I. Ifrim, J. Kabat, R. N. Germain, Histo-cytometry: A method for highly multiplex quantitative tissue imaging analysis applied to dendritic cell subset microanatomy in lymph nodes. *Immunity* **37**, 364–376 (2012). doi: 10.1016/j.immuni.2012.07.011; pmid: 22863836
76. N. Pagane, npagane/treg_specificity: Archived code for submission (published), Zenodo (2024); https://doi.org/10.5281/zenodo.14019650.
77. J. Arevalo *et al*., Evaluating batch correction methods for image-based cell profiling. *Nat. Commun.* **15**, 6516 (2024). doi: 10.1038/s41467-024-50613-5; pmid: 39095341
78. I. Korsunsky *et al*., Fast, sensitive and accurate integration of single-cell data with Harmony. *Nat. Methods* **16**, 1289–1296 (2019). doi: 10.1038/s41592-019-0619-0; pmid: 31740819
79. R. M. Quadros *et al*., *Easi*-CRISPR: A robust method for one-step generation of mice carrying conditional and insertion alleles using long ssDNA donors and CRISPR

ribonucleoproteins. *Genome Biol.* **18**, 92 (2017). doi: 10.1186/s13059-017-1220-4; pmid: 28511701
80. J. Shi, I. Getun, B. Torres, H. T. Petrie, Foxn1[Cre] expression in the male germline. *PLOS ONE* **11**, e0166967 (2016). doi: 10.1371/journal.pone.0166967; pmid: 27880796
81. J. J. Moon *et al*., Naive CD4$^+$ T cell frequency varies for different epitopes and predicts repertoire diversity and response magnitude. *Immunity* **27**, 203–213 (2007). doi: 10.1016/j.immuni.2007.07.007; pmid: 17707129
82. K. Tungatt *et al*., Antibody stabilization of peptide-MHC multimers reveals functional T cells bearing extremely low-affinity TCRs. *J. Immunol.* **194**, 463–474 (2015). doi: 10.4049/jimmunol.1401785; pmid: 25452566
83. F. P. Legoux, J. J. Moon, Peptide:MHC tetramer-based enrichment of epitope-specific T cells. *J. Vis. Exp.* **2012**, e4420 (2012). doi: 10.3791/4420-v; pmid: 23117190
84. T. Stuart *et al*., Comprehensive integration of single-cell data. *Cell* **177**, 1888–1902.e21 (2019). doi: 10.1016/j.cell.2019.05.031; pmid: 31178118
85. N. Pagane, Treg Specificity [Data set], Zenodo (2023); https://doi.org/10.5281/zenodo.8253629.

ACKNOWLEDGMENTS

We thank the University of Chicago Animal Resource Center for technical support with animal colonies; the University of Chicago Cytometry and Antibody Technology Facility (RRID:SCR_017760) for support with FACS experiments; the University of Chicago Genomics Facility (RRID:SCR_019196) for support with RNA sequencing, especially S. Arun for technical assistance and advice; the University of Chicago Transgenic Mouse and Embryonic Stem Cell Facility (RRID:SCR_019171) for creating *Tcaf3(exon5)*-floxed mice, especially L. Degenstein for performing microinjections and providing technical advice; the NIH Tetramer Core Facility (contract number 75N93020D00005) for providing tetramers, especially D. Long and R. Willis for technical advice; and members of the Savage and Kline laboratories for advice and discussions. We also thank D. Kasal for assistance in designing the *Tcaf3(exon5)*-floxed allele and technical advice and P. Penaloza-MacMaster, M.-L. Alegre, and W. Lisicka for support with pathogen techniques. We thank members of the Wong laboratory for helpful discussions and help with image processing and segmentation, particularly K. Nath and C. Skalnik. This report was prepared as an account of work sponsored by an agency of the United States Government. Neither the United States Government nor any agency thereof, nor any of their employees, makes any warranty, express or implied, or assumes any legal liability or responsibility for the accuracy, completeness, or usefulness of any information, apparatus, product, or process disclosed, or represents that its use would not infringe privately owned rights. Reference herein to any specific commercial product, process, or service by trade name, trademark, manufacturer, or otherwise does not necessarily constitute or imply its endorsement, recommendation, or favoring by the United States Government or any agency thereof. The views and opinions of authors expressed herein do not necessarily state or reflect those of the United States Government or any agency thereof. **Funding:** National Institute of Allergy and Infectious Diseases U01-AI154560 (P.A.S.); Chicago Biomedical Consortium Catalyst Award (P.A.S., N.E.F.); Institute for Translational Medicine Core Subsidy Award (P.A.S.); University of Chicago Interdisciplinary Training Program in Immunology T32-AI007090 (D.E.J.K., M.T.W., N.K.G., R.K.D.); US Department of Energy, Office of Science, Office of Advanced Scientific Computing Research, Department of Energy Computational Science Graduate Fellowship DE-SC0022158 (N.P.); National Institute of Health/National Cancer Institute predoctoral fellowship F30-CA236061 (C.H.M.); National Institute of Health/National Cancer Institute predoctoral fellowship F30-CA247264 (D.M.R.); University of Chicago Medical Scientist Training Program T32-GM007281 (C.H.M., D.M.R.); Intramural Research Program of NIAID, NIH (R.N.G.); Ragon Institute of Mass General, MIT and Harvard (H.S.W.); Mark and Lisa Schwartz Artificial Intelligence and Machine Learning Initiative (H.S.W.). **Author contributions:** Conceptualization: P.A.S., D.E.J.K., H.S.W., R.N.G.; Funding acquisition: P.A.S., H.S.W., R.N.G., N.E.F.; Investigation – original draft: D.E.J.K., N.P., C.H.M., M.T.W., N.K.G., D.M.R.; Investigation – review and editing: D.E.J.K., N.P., M.T.W., N.K.G., E.G.; Methodology: P.A.S., D.E.J.K., H.S.W., N.P., N.E.F., B.K.R.-P., R.K.D., E.J.A.; Project administration: P.A.S., H.S.W., R.N.G.; Software and data curation: N.P., M.M.-C.; Supervision: P.A.S., H.S.W., R.N.G.; Visualization: D.E.J.K., N.P., H.S.W., M.M.-C.; Writing – original draft and final manuscript: P.A.S., D.E.J.K., H.S.W., N.P., R.N.G. **Competing interests:** The authors declare that they have no competing interests. **Data and materials availability:** RNA-seq data are available at the NIH Gene Expression Omnibus under accession code GSE235974. Metadata used for the quantitative imaging analyses are available in Zenodo (*85*). All code and scripts used to analyze the quantitative imaging data are available in a GitHub repository (*76*). All other data needed to evaluate the conclusions are available in the main text or the supplementary materials. *Tcaf3 (exon5)^{floxed}* mice are available from P.A.S. under a material transfer agreement with the University of Chicago.

SUPPLEMENTARY MATERIALS

science.org/doi/10.1126/science.adk3248
Figs. S1 to S13
Tables S1 to S3
MDAR Reproducibility Checklist

Submitted 1 September 2023; resubmitted 16 September 2024
Accepted 17 December 2024
Published online 27 February 2025
10.1126/science.adk3248